

DEEP *Chandra* SURVEY OF THE SMALL MAGELLANIC CLOUD. II. TIMING ANALYSIS OF X-RAY PULSARS

JAESUB HONG^{1*}, VALLIA ANTONIOU¹, ANDREAS ZEAS^{2,3,1}, FRANK HABERL⁴, MANAMI SASAKI⁵, JEREMY DRAKE¹, PAUL PLUCINSKY¹, SILAS LAYCOCK⁶

¹Harvard-Smithsonian Center for Astrophysics, 60 Garden St., Cambridge, MA 02138, USA: jaesub@head.cfa.harvard.edu

²Foundation for Research and Technology-Hellas, 71110 Heraklion, Crete, Greece

³Physics Department & Institute of Theoretical & Computational Physics, University of Crete, 71003 Heraklion, Crete, Greece

⁴Max-Planck-Institut für extraterrestrische Physik, Giessenbachstraße, 85748 Garching, Germany

⁵University of Erlangen-Nurnberg/Remeis Sternwarte

⁶Department of Physics, University of Massachusetts Lowell, MA 01854, USA

Draft version October 12, 2018

ABSTRACT

We report the timing analysis results of X-ray pulsars from a recent deep *Chandra* survey of the Small Magellanic Cloud (SMC). We have analyzed a total exposure of 1.4 Ms from 31 observations over a 1.2 deg² region in the SMC under a *Chandra* X-ray Visionary Program. Using the Lomb-Scargle and epoch folding techniques, we have detected periodic modulations from 20 pulsars and a new candidate pulsar. The survey also covers 11 other pulsars with no clear sign of periodic modulation. The 0.5–8 keV X-ray luminosity (L_X) of the pulsars ranges from 10^{34} to 10^{37} erg s⁻¹ at 60 kpc. All the *Chandra* sources with $L_X \gtrsim 4 \times 10^{35}$ erg s⁻¹ exhibit X-ray pulsations. The X-ray spectra of the SMC pulsars (and high mass X-ray binaries) are in general harder than those of the SMC field population. All but SXP 8.02 can be fitted by an absorbed power-law model with a photon index of $\Gamma \lesssim 1.5$. The X-ray spectrum of the known magnetar SXP 8.02 is better fitted with a two-temperature blackbody model. Newly measured pulsation periods of SXP 51.0, SXP 214 and SXP 701 are significantly different from the previous *XMM-Newton* and *RXTE* measurements. This survey provides a rich data set for energy-dependent pulse profile modeling. Six pulsars show an almost eclipse-like dip in the pulse profile. Phase-resolved spectral analysis reveals diverse spectral variation during pulsation cycle: e.g., for an absorbed power-law model, some exhibit an (anti)-correlation between absorption and X-ray flux, while others show more intrinsic spectral variation (i.e., changes in photon indices).

1. INTRODUCTION

The Small Magellanic Cloud (SMC) is a dwarf irregular satellite of the Milky Way. Located nearby (~ 60 kpc, Hilditch et al. 2005) with a relatively unobstructed view ($N_H \sim 10^{21}$ cm⁻²), the SMC is an ideal place to study stellar evolution as it is experiencing an era of intense star formation ($0.05\text{--}0.4 M_\odot \text{ yr}^{-1}$, Harris & Zaritsky 2004; Shtykovskiy & Gilfanov 2005), which is likely triggered by the tidal interaction with the Large Magellanic Cloud (LMC) and our Galaxy (Zaritsky & Harris 2004). The SMC harbors a large population of young X-ray binaries (XRBs), dominantly in forms of High Mass XRBs (HMXBs) with Be star companions. Thus, the SMC hosts an usually high number of Be-XRBs (e.g., Coe & Kirk 2015; Haberl & Sturm 2016; Antoniou & Zezas 2016), which is likely linked to the recent star formation episode and low metallicities in the region (e.g., Antoniou et al. 2010).

In Be-XRBs, the compact object, a spinning neutron star (NS), accretes the material from the circumstellar disk of the Be star, triggering bright X-ray outbursts with typical X-ray luminosity of $\sim 10^{36\text{--}37}$ erg s⁻¹. Long-term monitoring surveys of the SMC with *RXTE* (e.g., Laycock et al. 2005; Galache et al. 2008) detected more than 50 pulsars during outbursts, predominantly in the SMC Bar. Observations with *XMM-Newton* (e.g., Sturm et al. 2013) and *Chandra* (e.g., Laycock et al. 2010) have also detected dozens of new pulsars in the region, and also extended the detection of XRBs to the quiescent

regime ($\sim 10^{33}$ erg s⁻¹).

In order to establish a full census of all active accreting binaries down to $L_X \sim 10^{32}$ erg s⁻¹, a deep *Chandra* survey of the 11 fields in the SMC was recently conducted under a *Chandra* X-ray Visionary Program (PI. A. Zezas). The goal of the survey is to acquire the deepest X-ray luminosity function (XLF) in the region, and thus to measure the formation efficiency of XRBs as a function of age, and the evolution of the XLF, which can be used to constrain the XRB population synthesis models. The details of the survey program along with the full source catalog are found in Antoniou et al. (2017, in preparation).

These deep *Chandra* observations provide the spectral and timing information for the SMC X-ray pulsars (SXPs) with unprecedented high precision thanks to the low background enabled by the superb angular resolution of the *Chandra* X-ray observatory. In this paper, we report the X-ray timing analysis results of the SXPs from our *Chandra* survey. In §2 we outline the observations and analysis pipeline for source search and aperture photometry. In §3 we describe the procedures for timing analysis and the phase-resolved spectral analysis using spectral model fitting, energy quantiles and energy-versus-phase diagrams. In §4 we present the pulsation search results and review the properties of each pulsar that exhibited X-ray pulsations during our survey. In §5 we compare the properties of pulsars with those of other HMXBs and general field sources in the SMC, and

summarize the interesting features of selected pulsars.

2. OBSERVATIONS AND DATA PROCESSING

We have conducted a *Chandra* survey of seven and four fields in the Bar and Wing regions of the SMC, respectively, from 2012 December to 2014 March with a total exposure of 100 ks per each field. Back in 2001 and 2006, three other fields in the SMC Bar were observed with *Chandra* also for 100 ks each. We have analyzed all 14 deep *Chandra* fields for the timing analysis of the SMC pulsars. Table 1 summarizes the deep *Chandra* observations of the SMC fields analyzed in this paper and the source count in each field.

Each deep field overlaps with its neighboring fields to varying degrees. Except for the observation of the NGC346 field (Obs. ID 1881), the 100 ks exposure of each field was broken into two (and in a few cases three) segments in part due to the observing constraints of *Chandra*. The sensitivity of pulsation detection improves when combining multiple observations unless they are far apart in time, which can introduce phase mixing. Thus, when a field is repeatedly observed within a week or two, we stack the observations for pulsation search. For instance, Deep Field 3 (DF3) was observed on three separate occasions (Obs. IDs 14666, 15499, and 16490) and for the timing analysis, we stack the last two of these observations (Obs. IDs 15499 and 16490) after separate searches in individual observations. Table 2 lists the run-down source counts in the stacked fields.

For the analysis of both the individual observations and the stacked data we employed the latest version of the X-ray analysis pipeline developed for the *Chandra* Multi-wavelength Plane survey (ChaMPlane; Grindlay et al. 2005; Hong 2012). The ChaMPlane pipeline is independent of the analysis pipeline used in Antoniou et al. (2017, in preparation), but the former was chosen for timing analysis because of its proven maturity of periodicity search and subsequent analysis tools (e.g., Hong et al. 2009; Laycock et al. 2010; Hong et al. 2012). Since a reliable timing analysis requires at least moderately bright sources with $\gtrsim 100$ net counts, the minor differences between the two pipelines that only matter for relatively faint sources ($\lesssim 20$ net counts) do not change the outcome of this analysis.

The latest version of the ChaMPlane pipeline is based on CXC CIAO version 4.6 or later. In summary, we searched for point sources using *wavdetect* (Freeman et al. 2002) in the 0.5–7 keV band¹ and performed the aperture photometry in multiple energy bands to extract basic X-ray properties such as net counts, energy quantiles, X-ray fluxes and luminosities. For bright sources with ≥ 100 net counts in the 0.3–8 keV band, we searched for periodic X-ray modulation (§3). We have detected 2339 X-ray point sources from 31 individual pointings, and have found periodic modulations from 18 sources among 244 bright sources. In the stacked data sets, we have detected 458 X-ray point sources and found 10 periodic sources among 52 bright sources. The last three columns

¹ For source detection we chose a section of the broad band (0.3–8 keV) used for the photometry, where the *Chandra* ACIS-I chips are most sensitive. This is to detect all the bright sources efficiently regardless of their spectral hardness without need for additional source searches in separate soft and hard bands.

in Tables 1 and 2 summarize source counts from individual and stacked data sets, respectively. Note that source counts in Table 1 include many duplicate sources from the repeated observations.

3. TIMING ANALYSIS

3.1. Initial Search with Lomb-Scargle Periodograms

We have searched for periodic X-ray modulations in the 296 sources with ≥ 100 net counts in the 0.3–8 keV band from 31 individual observations and 5 stacked data sets. For each source, we applied barycenter corrections on the arrival times of source and background events, and then generated a background subtracted light curve in the 0.3–8 keV band with a bin size of 3.14 s. We created a Lomb-Scargle (LS) periodogram (Scargle 1982) from each light curve over a wide range of search periods.

We determined independent search periods based on the overall observation duration and the number of net counts. We followed the recipe by Horne & Baliunas (1986), where the number of the independent search frequencies (N_f) is given as $-6.362 + 1.193 N_E + 0.00098 N_E^2$ and N_E is the net counts of the source. We selected N_f periods from $2T_D/N_E$ to T_D at an equal frequency spacing, where T_D is the observation duration. For example, a source with 1000 net counts observed in 100 ks would require a search of 2167 independent periods from ~ 100 s to 50 ks at a frequency interval of ~ 4.3 μ Hz. In order to ensure a successful search, we refine the frequency spacing further by a factor of two (i.e. ~ 2.2 μ Hz for the above example). In addition, we extend the search periods down to ~ 6 sec, given the large population of sub 100 sec period pulsars in the region. We keep the same frequency spacing when adding new periods. In the above example, then, we would have scanned $\sim 87,000$ periods and roughly a half of them would be independent.

The false detection probability (P_{FD}) can be calculated from the amplitude (X) of the LS periodogram and the total number of search periods ($N_T = \sum_i N_{f,i}$ where $N_{f,i}$ is the the number of search periods for source i) as $P_{FD} = 1 - (1 - e^{-X})^{N_T}$. We have searched about 7×10^6 independent periods from the 296 sources in total, and corresponding 1%, 5% and 10% false detection probabilities are at $X \sim 20.4, 18.7$ and 18.0 respectively. To be conservative, we follow up on all the periods with $X > 16.5$ ($P_{FD} \sim 50\%$) for further analysis. All of the observations analyzed in this paper were conducted in the normal *Chandra* ACIS readout mode where the CCD readout cycle time of $\sim 3.14 - 3.24$ s fundamentally limits the search for modulation periods $\lesssim 10$ s. Therefore, the above estimates of P_{FD} are somewhat conservative.

Sources that are observed in a region with a noticeable exposure variation ($\gtrsim 10$ –20%; e.g., near an edge of a CCD or a section with a large CCD column-to-column efficiency variation) can exhibit false modulations due to dithering motions. We excluded the known false periods (707 s and 1000 s) and their harmonics from further investigation.

3.2. Refining Pulsation Search with Epoch Folding

To acquire precise modulation periods, we refined the initial search results by performing the epoch folding (EF) search (Leahy et al. 1983) and repeating the LS search for 1000 equally spaced periods within the full-

Table 1
Chandra Observations of the SMC

(1) Obs. ID	(2) DF ID	(2) Stacked for Period Search	(3) Pointing (J2000)		Start Time (UT)	Exposure (ks)	(3) GTI (ks)	(4) Total 0.5–7 keV	(5) Source Count		(6) Periodic Sources
			R.A. (h m s)	Dec ($^{\circ}$ $'$ $''$)					Net ≥ 100 0.3–8 keV	Periodic Sources	
1881			00 59 05.0	-72 10 42.1	2001-05-15 01:54	100.0	98.7	136	28	4	
7155	01A	1	00 53 34.5	-72 26 43.2	2006-04-25 05:15	50.0	49.3	109	14	2 (2)	
7327	01A	1	00 53 34.5	-72 26 43.2	-04-26 14:57	50.0	47.4	100	8	3 (2)	
8479	02A	2	00 50 41.4	-73 16 10.3	-11-21 12:03	45.0	42.1	68	10	4 (3)	
7156	02A	2	00 50 41.4	-73 16 10.3	-11-22 18:48	39.0	38.7	77	9	3 (3)	
8481	02A	2	00 50 41.4	-73 16 10.3	-11-23 15:45	16.0	16.0	43	6	1 (1)	
14666	03		01 13 56.9	-73 20 34.0	2012-12-28 14:49	50.0	49.4	79	12		
14668	05		00 56 08.6	-72 35 02.5	2013-01-02 12:22	50.0	49.4	92	10	1 (1)	
14670	07		00 51 52.0	-73 00 24.6	-01-06 17:52	50.0	49.4	75	5	1	
14671	08		00 56 35.9	-72 20 06.3	-01-07 08:18	50.0	48.1	94	19		
14667	04		01 13 39.9	-73 08 37.2	-01-15 09:43	50.0	46.5	56	5		
14672	09		00 49 43.2	-72 49 16.3	-01-17 16:09	50.0	44.8	77	10	1	
14673	10		00 41 00.0	-73 20 00.0	-01-18 08:02	50.0	44.8	86	5	1	
14674	11		00 47 09.6	-73 07 33.0	-03-04 22:33	50.0	45.9	71	10	2 (1)	
14665	02		01 13 33.2	-72 32 41.8	-03-09 05:11	50.0	47.8	89	7		
14669	06		00 52 46.6	-72 42 11.8	-03-11 07:15	50.0	47.4	65	4		
14664	01		01 11 10.1	-72 44 03.5	-03-25 02:20	50.0	49.4	75	3		
15501	05		00 56 08.6	-72 35 02.5	-06-25 19:11	50.0	48.1	98	10	1 (1)	
15498	02		01 13 33.2	-72 32 41.8	-08-09 00:04	50.0	49.4	87	9		
15500	04		01 13 39.9	-73 08 37.2	-08-24 21:07	50.0	49.4	67	8		
15502	06		00 52 46.6	-72 42 11.8	-08-26 11:44	50.0	45.8	63	4		
16320	01	3	01 11 10.1	-72 44 03.5	-08-30 03:28	32.0	29.7	59	1		
15497	01	3	01 11 10.1	-72 44 03.5	-08-31 16:27	18.0	17.8	43	1		
15504	08		00 56 35.9	-72 20 06.3	-09-06 01:43	50.0	48.8	98	15	1	
15507	11	4	00 47 09.6	-73 07 33.0	-09-13 16:37	25.0	24.7	44	4	1 (1)	
16367	11	4	00 47 09.6	-73 07 33.0	-09-25 14:39	25.0	24.0	45	4	1 (1)	
15499	03	5	01 13 56.9	-73 20 34.0	-10-14 22:57	25.0	24.0	46	4		
16490	03	5	01 13 56.9	-73 20 34.0	-10-15 20:36	25.0	24.2	46	2		
15505	09		00 49 43.2	-72 49 16.3	2014-01-15 11:21	50.0	48.4	88	7	1	
15506	10		00 41 00.0	-73 20 00.0	-02-28 16:49	50.0	49.4	76	5		
15503	07		00 51 52.0	-73 00 24.6	-03-12 14:26	50.0	45.4	87	5		
Total						1400.0	1344.3	2339	244	18	

Notes. (1) Deep Field (DF) designation ID. (2) Stacked observations for timing analysis. (3) Good time intervals (GTIs). (4) The number of sources detected by the *wadetect* routine in the 0.5–7 keV band (Freeman et al. 2002). (5) Sources with ≥ 100 net counts in the 0.3–8 keV band. (6) The number of periodic sources. The number in the parenthesis indicates duplicate sources detected in the other repeated observations.

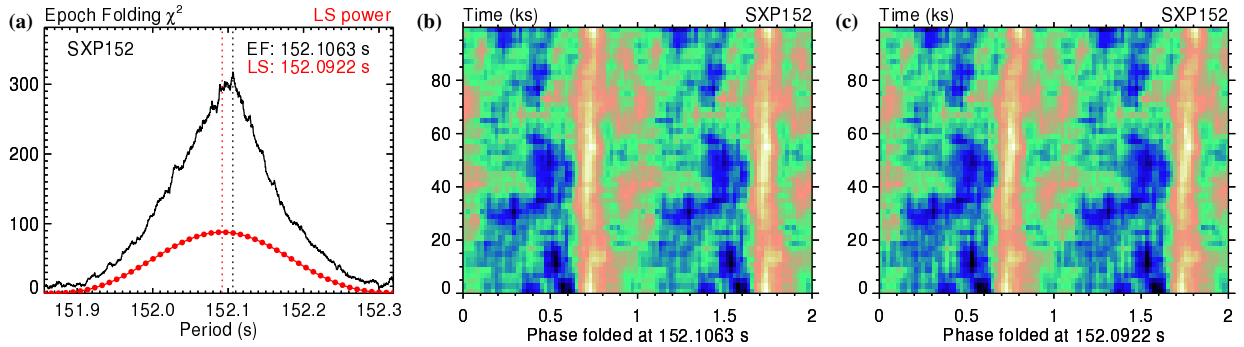


Figure 1. Searching for the true modulation period of SXP 152 between the peak periods of the refined LS (red) and EF (black) periodograms (a) using the time versus phase diagrams (b and c). Darker (bluer) and lighter (yellow) colors in the time versus phase diagrams indicate relatively high and low counts, respectively. Unlike the peak period of the EF periodogram (b), the peak period of the LS periodogram (c) shows a noticeable phase drift: the minimum is near phase ~ 0.7 at $T \sim 0$ and near phase ~ 0.8 at $T \sim 100$ ks.

Table 2
Analysis of Five Stacked Fields in the SMC

(1) DF ID	(2) Stacked Obs.	Exp. (ks)	(3) GTI (ks)	(5) Source Count		
				Total 0.5–7 keV	Net ≥ 100	Periodic Sources
01A	7155, 7327	100.0	93.8	131	20	5
02A	7156, 8479, 8481	100.0	96.7	118	19	4
01	16320, 15497	50.0	47.5	78	4	1
11	15497, 16320	50.0	48.7	66	4	1
03	15499, 16490	50.0	48.2	65	5	
Total		350.0	334.9	458	52	10

See the notes in Table 1.

width half maximum (FWHM) of the candidate periods from the initial search. In the EF search, for a given search period, we folded the source and background events in the 0.3–8 keV band in 15 equal phase bins. The background-subtracted net counts in the folded bins were

converted to the folded light curve using the summed good time intervals (GTIs) of each phase bin. The reduced χ^2 of the folded light curve with respect to the constant rate was calculated to generate periodograms of the EF searches.

For a given initial candidate pulsation period, the refined LS and EF periodograms present two new refined candidates, which do not necessarily agree with each other. To find the accurate modulation period, we visually inspected the skewness of the X-ray event distribution in the time versus phase diagrams at the two periods, and also compared the modulation amplitudes and pulsed fractions of the two periods. If one of the two periods shows a noticeable skewness in the time versus phase diagram, the other period is chosen to be the correct

modulation period. If neither of the two periods shows any significant skewness, the period with a higher modulation amplitude or a higher pulsed fraction (or both) is selected. When the difference in the modulation amplitude and pulsed fraction is marginal, we accept the result of the LS periodogram.

The modulation amplitude (A_{mod}) is defined as $1 - r_{\text{min}}/r_{\text{max}}$ where r_{min} and r_{max} are the minimum and maximum of the folded light curve, respectively. The pulsed fraction (P_F) is calculated as the ratio of the pulsating flux above the minimum to the total flux, i.e., $\sum_i (r_i - r_{\text{min}})/\sum_i r_i$, where r_i is the count rate of the folded bin i . In calculating A_{mod} and P_F , we change the number of the folded bins according to the total net counts in order to limit the statistical fluctuation due to low count bins. Each folded bin should contain at least 25 net counts on average, but the total number of the folded bins is no more than 20: e.g., 5, 10, 15, and 20 phase bins for 125, 250, 375, and > 500 count sources, respectively. In order to avoid aliasing effects of binning, we generate multiple folded light curves by varying the starting phase of folded bins and take the average results of the multiple light curves for A_{mod} and P_F .

Figure 1 illustrates the selection process of the modulation period for SXP 152 as an example. Panel (a) compares the EF (black) and LS (red) periodograms. Panels (b) and (c) show the X-ray event distribution in the elapsed observation time versus phase diagrams folded at the peak periods of the EF and LS periodograms, respectively. Two cycles are shown for easy viewing. In SXP 152, the peak period of the LS periodogram (c) shows a noticeable drift of the minimum phase (from phases ~ 0.7 at the early times to phases ~ 0.8 at the late times), whereas the peak period of the EF periodogram does not (b). Therefore, the pulsation period for SXP 152 is determined to be 152.1063 ± 0.0094 s.

The uncertainty of a modulation period is often estimated by an 1σ equivalent spread of the peak in the periodogram. Instead we follow the recipe given by Horne & Baliunas (1986). The error estimates by the latter tend to be tighter than those by the former. Our analysis finds that the two peak periods of the refined LS and EF periodograms are always consistent with each other within only a tiny fraction of the uncertainty estimate by the former. On the other hand, in some cases, the visual inspection of skewness in the time versus phase diagram clearly shows that one of the two periods has a noticeable skewness. Therefore, we conclude that the former approach is too conservative and the latter produces more appropriate error estimates. In the example shown in Figure 1, the two peak periods of the EF and LS periodograms are within 0.2σ and 1.5σ of each other under the peak width-based error (0.058 s) and the uncertainty estimate (0.0094 s) by the recipe in Horne & Baliunas (1986), respectively.

3.3. Phase-Resolved Spectral Analysis

We used energy-band dependent folded light curves, energy versus phase diagrams, phase-segmented spectral fits and energy quantiles for phased-resolved spectral analysis of the SMC pulsars. For relatively brightest sources with $\gtrsim 1000$ net counts, we performed spectral model fits of a few selected phase segments in order to constrain the spectral parameters and their changes more

precisely. Similarly to the overall spectral model fits, except for the magnetar SXP8.02, phase-resolved spectra of all the bright sources are better fitted by an absorbed power-law model.

For fainter sources, X-ray color-color diagrams are often used for the evaluation of two-parameter models for X-ray spectra with poor statistics. X-ray colors or hardness ratios, however, suffer a spectral bias intrinsic to the sub-energy band selection. The Bayesian Estimation of Hardness Ratio (BEHR, Park et al. 2006) alleviates the intrinsic bias to some degree through a rigorous probabilistic treatment. We use energy quantile diagrams consisting of median energy and quartile ratio, which enable a bias-free evaluation of the two-parameter spectral models (Hong et al. 2004).

Equal-count phase bins were used for phase-resolved energy quantile calculation in order to maintain roughly similar photon statistics among different phase bins and thus acquire a reliable estimate of energy quantiles for each phase bin. For a given phase of a pulsation period, we first calculate the width of each phase bin to include ≥ 50 net counts, and estimate the energy quantiles of the phase bin accordingly. We repeat the calculation for 100 different phase bins for every pulsar, where the number of the independent bins is given as $\min[\sim N_c/50, 100]$ with N_c the total net counts. We explore whether the spectral variation, if any, is intrinsic or absorption dependent through the phase-resolved quantile diagram.

We also use the energy versus phase diagrams to visualize diverse spectral changes over pulsation cycles.² Folded-light curves in the three energy bands also illustrate the spectral variation over pulsation cycles.

4. PULSATION SEARCH RESULTS

Table 3 summarizes our pulsation search results, which are grouped into three categories: (candidate) pulsars exhibiting solid, marginal, and no pulsations during our survey. All the periodic modulations are from the known pulsars except for a relatively marginal detection of periodicity at 7.59 s from CXOU J003942.37-732427.4. SXP 51.0, SXP 214 and SXP 701 show notable deviations in the periods from the reported values in the literature (see below and Hong et al. 2016). SXP 25.5 and SXP 51.0 are identified as the same source with the latter representing the proper spin period.

For the pulsars exhibiting no significant periodic modulations in the LS periodograms, we manually performed the EF searches and calculate the upper limit of A_{mod} around the known pulsation periods. For the known pulsars that were not detected in our source search, we estimated the upper limit of the flux and luminosity based on the background counts in the 95% point spread function (PSF) around the source position. Flags in Table 3 indicate sources with the following possible spectral variations based on phase-resolved quantile diagrams: "i" for intrinsic variation (i.e., changes in Γ for an absorbed power-law model) and "a" for changes more likely in absorption (N_H).

² For energy versus phase diagrams, we ignore the background counts. This is acceptable for bright SMC pulsars because of the relatively low background in a small aperture of each source region, which is enabled by the superb angular resolution of the *Chandra* X-ray optics.

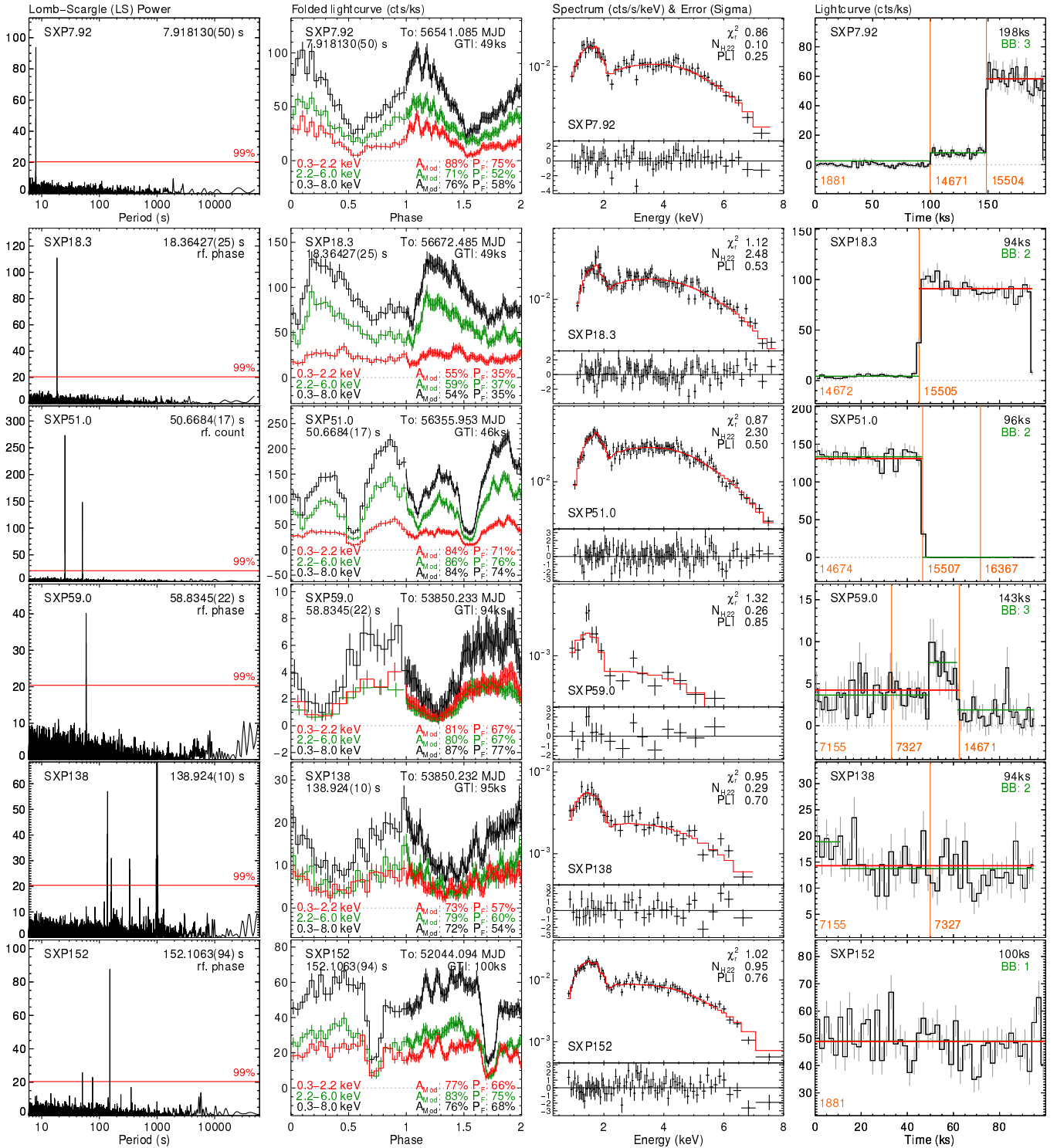


Figure 2. LS periodograms, folded light curves, energy spectra, and compressed light curves (i.e., without observational gaps) of the periodic X-ray sources of SXP 7.92, SXP 18.3, SXP 51.0, SXP 59.0, SXP 138 and SXP 152. The periodograms are shown with the 99% confidence levels (red horizontal lines, Section 3.1). The labels ‘rf. phase’ and ‘rf. count’ indicate that the pulsation period is selected from the refined EF search instead of the LS periodogram (Section 3.2). The folded light curves are drawn for the 0.3–8 keV (black), 0.3–2.2 keV (red), and 2.2–6 keV (green) bands along with A_{mod} and P_F . In the energy spectra, the best-fit power-law models are shown in (red) lines. In the compressed light curves, the (red) horizontal lines represent the average count rate of the observation(s) exhibiting the periodicity and they indicate the observation(s) used for the folded light curves and spectral fits (e.g., Obs. IDs 7155 and 7327 for SXP 59.0), while the (green) steps show the Bayesian Blocks (BBs) calculated from the unsubtracted event list without observational gaps. The number of BBs are labeled on the right-upper corner of each panel.

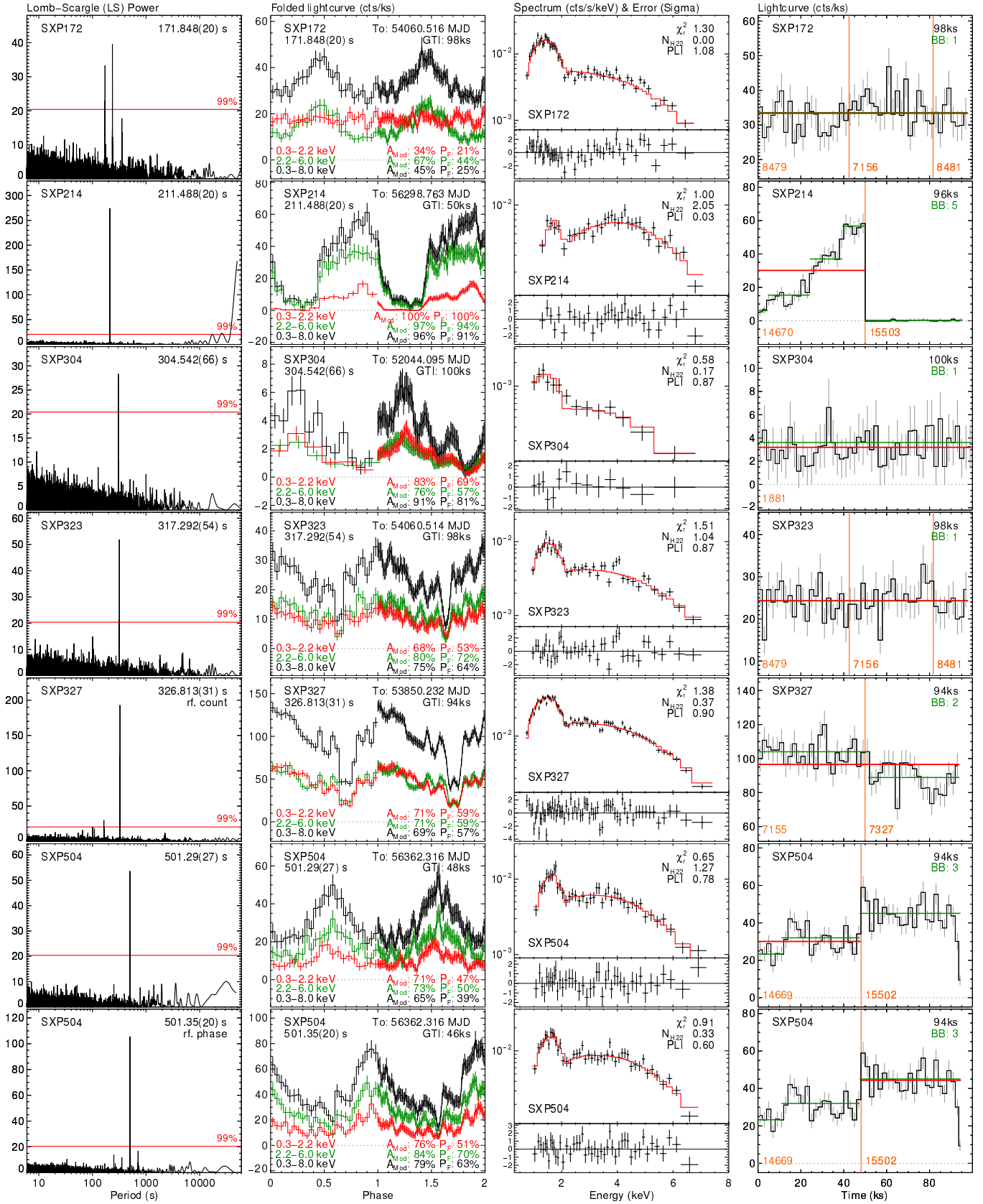


Figure 3. Same as Figure 2 for SXP 172, SXP 214, SXP 304, SXP 323, SXP 327 and SXP 504. In SXP 504, the results of two observations (Obs. IDs 14669 and 15502) are shown.

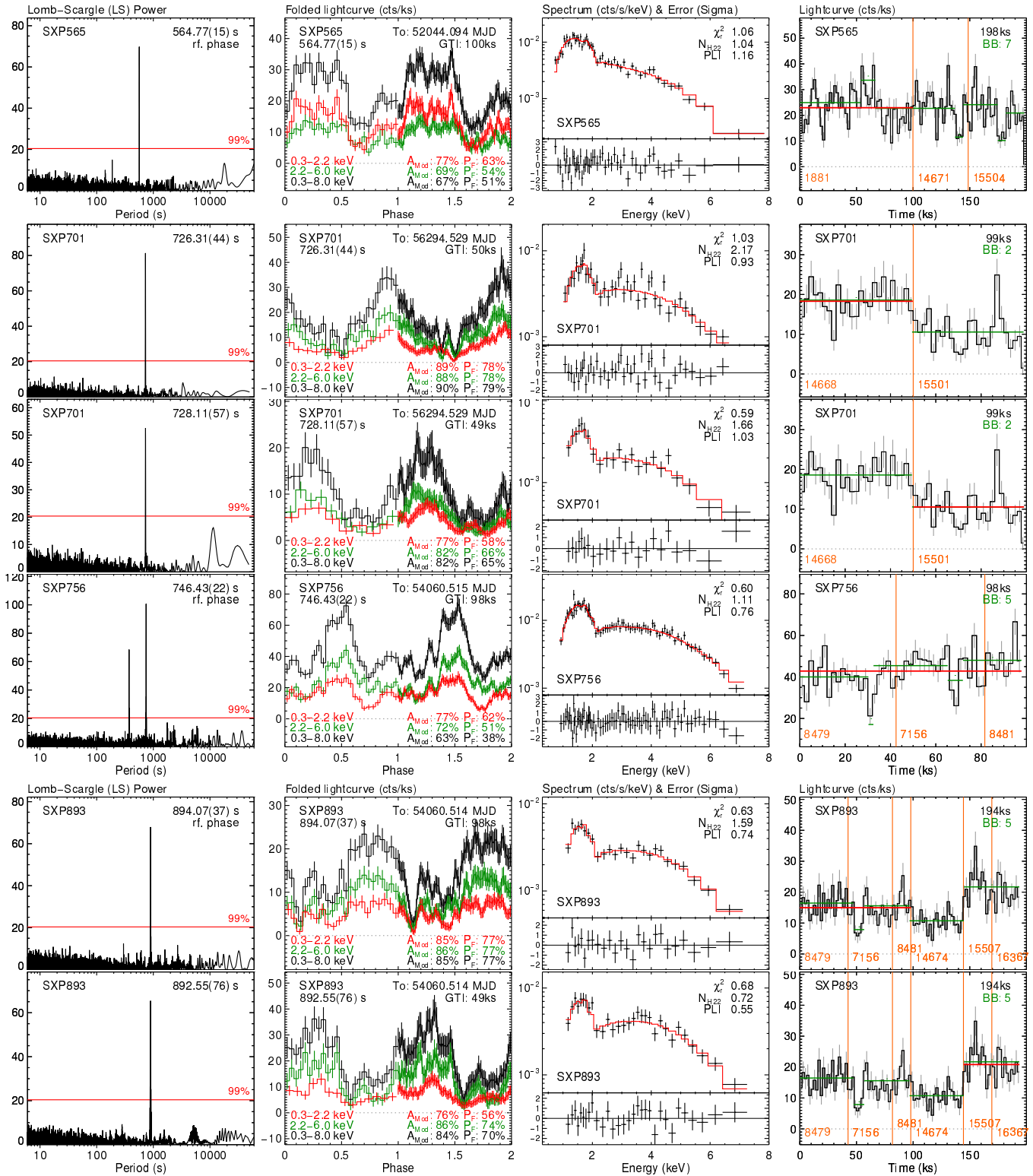


Figure 4. Same as Figure 2 for SXP 565, SXP 701, SXP 756, and SXP 893. In SXP 701 and SXP 893, the results of two sets of observations are shown: Obs. IDs 14668 and 15501 for SXP 701; Obs. IDs 8478, 7156, 8481 and Obs. IDs 15507, 16367 for SXP 893 (see Table 3).

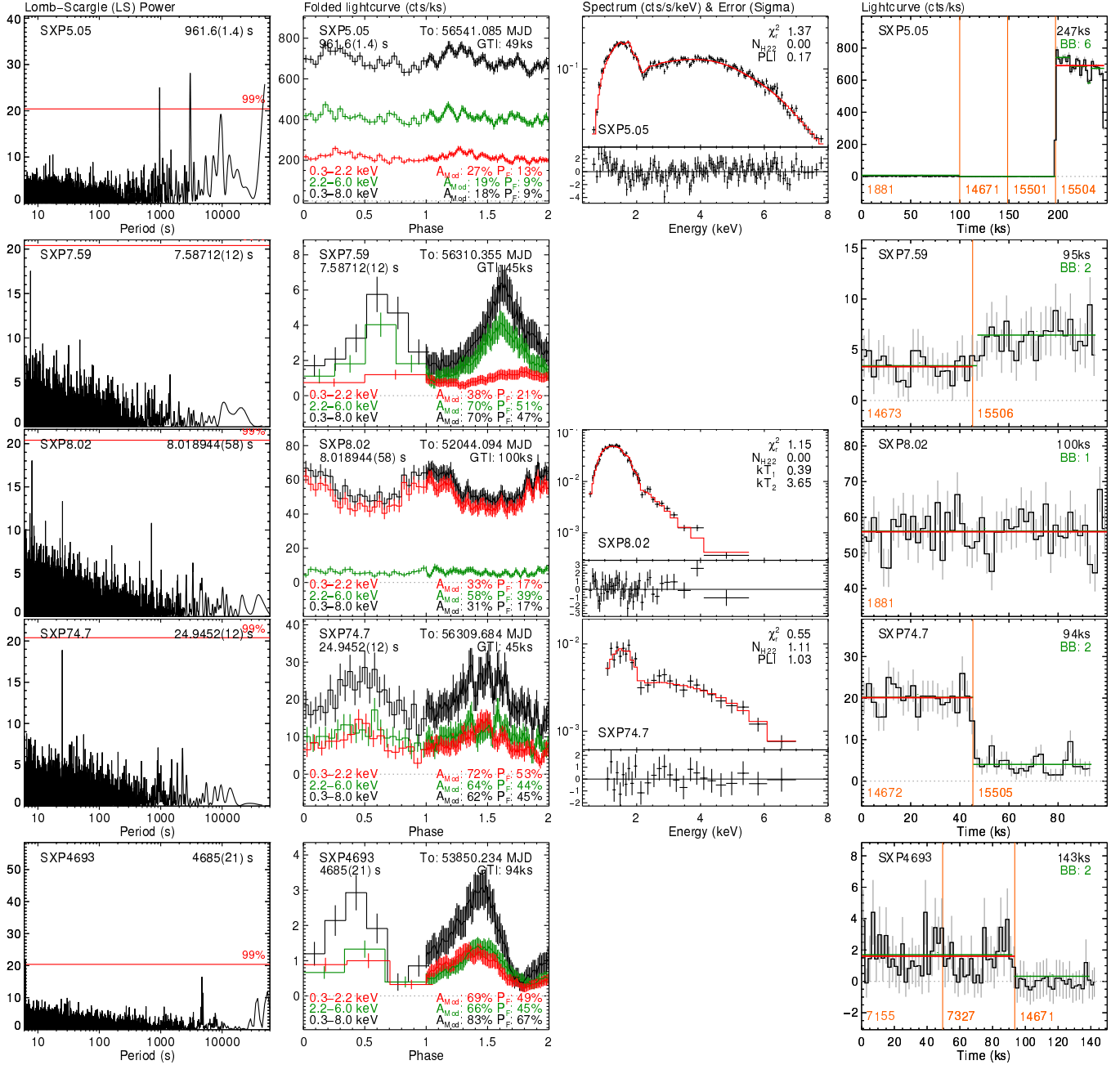


Figure 5. Same as Figure 2 for SXP 5.05, SXP 7.59, SXP 8.02 and SXP 74.7 and SXP 4693. An absorbed two-temperature blackbody model is used for spectral model fit for SXP 8.02. For spectral analysis of relatively low count sources (SXP 7.59 and SXP 4693, ~ 150 net counts), we rely on quantile analysis instead of spectral model fitting (Table 4).

Among the pulsars without no pulsations observed with *Chandra*, the identification of SXP 9.13 as the *ROSAT* source RX J0049.5-7311 is in question due to lack of pulsations from the source even though the source was observed with *XMM-Newton* and *Chandra* many times (see Haberl & Sturm 2016). Its pulsation was originally discovered from the *ASCA* source AX J0049-732. According to the source position in the catalogue by Coe & Kirk (2015), SXP 280 should have been covered by the *Chandra* observation (Obs ID. 1881), but Haberl & Sturm (2016) showed that its optical counterpart is located outside of the *Chandra* field of view. Therefore, SXP 280 is excluded in the list.

Figures 2–5 show the LS periodograms, the folded light curves, the overall spectra with model fits, and the compressed light curves (without observational gaps) of the 21 SMC pulsars exhibiting pulsations during our survey. The LS periodograms cover ~ 5 s to ~ 50 ks, and the red horizontal line indicates a confidence level of 99% ($P_{FD} = 1\%$). The folded light curves of the equal phase bins are shown in the three energy bands (black: 0.3–8 keV, red: 0.3–2.2 keV, green: 2.2–6 keV) for two cycles: the first cycle (phase 0 to 1) is shown with independent phase bins, whereas the second cycle (phase 1 to 2) is shown in a sliding window of phase bins.

For spectral model fits, we have tried an absorbed power-law, thermal bremsstrahlung, blackbody, and APEC models with two absorption components: the Galactic foreground absorption of $N_{\text{H}} = 6 \times 10^{20} \text{ cm}^{-2}$ (Dickey & Lockman 1990) with solar abundance ($Z = Z_{\odot}$), and the free SMC local absorption with $Z = 0.2 Z_{\odot}$ (Russell & Dopita 1992) using the absorption model by Wilms et al. (2000). All except for SXP 8.02 are best fitted by an absorbed power-law model with $\Gamma \lesssim 1.5$ among the four models considered here. SXP 8.02, a magnetar, is better fitted with a two-temperature blackbody model (Section 4.19). Table 4 summarizes the spectral properties of the 31 SMC pulsars covered in the survey, which also includes all the results from the observations even when no pulsations were detected.

The compressed light curves show the changes in the background-subtracted event rates without observational gaps. The average rate during the observation(s) exhibiting the pulsation is shown in red, and the green segments show the average rate of the independent Bayesian Blocks (BBs), which mark the change points between time intervals of statistically different rates (Scargle et al. 2013).

Below we explore the X-ray properties of each SXP that exhibited X-ray modulations during the *Chandra* observations. X-ray luminosities quoted in the following sections refer to the observed values in the 0.5–8 keV band, assuming a distance of 60 kpc unless specified otherwise. Table 4 lists both the observed and intrinsic X-ray luminosities.

4.1. SXP 7.92

SXP 7.92 was first identified as a pulsar from an *RXTE* observation by Corbet et al. (2008). Coe et al. (2009) suggested the early-type star AzV285 with a spectral type of O9-B0 III as the counterpart.

SXP 7.92 was observed with *Chandra* once in 2001 and twice in 2013. In 2001, the source was positioned in ACIS-S3, far off the aimpoint, and it was not detected with an upper limit (3σ) of the 0.5–8 keV X-ray luminos-

ity at $2.4 \times 10^{33} \text{ erg s}^{-1}$ for an absorbed power-law model (see below for the model parameters). We detected the source with an X-ray luminosity of $\sim 10^{35} \text{ erg s}^{-1}$ in the 2013 January observation, but no pulsation was observed ($A_{\text{mod}} \lesssim 46\%$). The observation eight months later showed that the X-ray luminosity had increased to $7.5 \times 10^{35} \text{ erg s}^{-1}$, and a significant pulsation was detected. The LS periodogram shows strong peaks at 5.5088 and 7.9181 s, and the former is the result of beating between the pulsation period (the latter) and the CCD readout cycle (~ 3.14 s). The observed luminosity is still lower than what *Swift* observed in 2008 by an order of magnitude (Coe et al. 2009), indicating the large flux changes over four orders of magnitudes.

The overall X-ray spectrum (Obs. ID 15504) is well fitted by an absorbed power-law model with $\Gamma = 0.25 \pm 0.06$ and $N_{\text{H}} = 10^{21} \text{ cm}^{-2}$. The relatively hard *Chandra* spectrum is consistent with the quantile analysis from the 2008 *Swift* data by Coe et al. (2009). The X-ray spectrum did not show any significant change between the two observations in 2013. Despite the relatively short period that can cause the phase mixing for the given CCD readout cycle, the pulse profile shows a large modulation amplitude ($A_{\text{mod}} \sim 76\%$). The pulse profile of SXP 7.92 is known to transition between the single peak and two peak shapes (Coe et al. 2009). The pulse profile measured with *Chandra* shows a single peak similar to what the 2004 *RXTE* observation detected (Coe et al. 2009), but, given the short pulsation period, the long CCD readout cycle in the *Chandra* ACIS chips may have contributed to the apparent single peak profile. The phase-resolved quantile diagram shows a marginal variation in the X-ray absorption but no apparent correlation with the flux.

4.2. SXP 18.3

X-ray pulsations from SXP 18.3 were first found with *RXTE* in 2003 by Corbet et al. (2003). The position of the source was later localized with *XMM-Newton* by Eger & Haberl (2008). The OGLE-III optical light curve revealed a coherent period of ~ 18 d (Udalski & Coe 2008).

The source was observed with *Chandra* in January of 2014 and 2015. Between the two observations, the X-ray luminosity increased from 3.8×10^{34} to $10^{36} \text{ erg s}^{-1}$. The latter is still lower than what was observed during the 2007 *XMM-Newton* observation (Eger & Haberl 2008) or the average X-ray luminosity seen with *RXTE* (Klus et al. 2014) by a factor of ~ 6 – 7 . The X-ray pulsation is not detected in the 2014 observation ($A_{\text{mod}} \lesssim 66\%$), and the pulsation period detected in the 2015 observation ($A_{\text{mod}} \sim 54\%$) is consistent with the long-term spin-up trend reported by Klus et al. (2014).

The X-ray spectrum, well fitted by an absorbed power-law model with $\Gamma = 0.53 \pm 0.06$ (Figure 2), remained consistent between the *XMM-Newton* and two *Chandra* observations. The phase-resolved quantile diagram in Figure 6(a) shows a marginal correlation between the absorption and the flux, where a heavier absorption is present during phases of higher fluxes. The spectral fits of the two selected phases representing the peak (phases 0.15–0.35) and valley (phases 0.7–1.0) of the folded light curve show similar results (Figure 6(b)). Table 5 summarizes the best-fit spectral parameters.

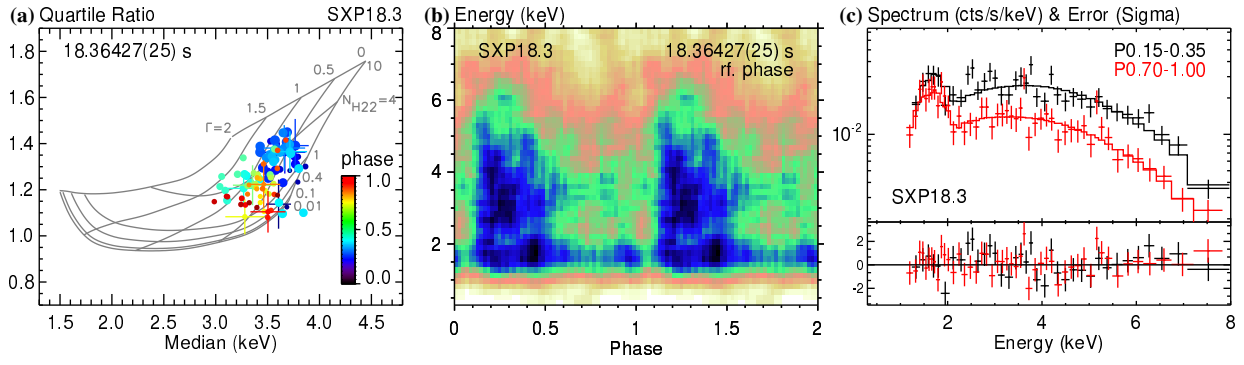


Figure 6. Phase-resolved quantile diagram, energy versus phase diagram and spectral model fits of SXP 18.3. See Section 4.2. The data points in the quantile diagrams are color-coded by pulsation phases (i.e., purple at phase ~ 0.0 and red at phase ~ 1.0), and the grids are for absorbed power-law models with $\Gamma = 0, 0.5, 1, 1.5,$ and 2 , and $N_{\text{H}} = 0.01, 0.1, 0.4, 1, 4,$ and $10 \times 10^{22} \text{ cm}^{-2}$.

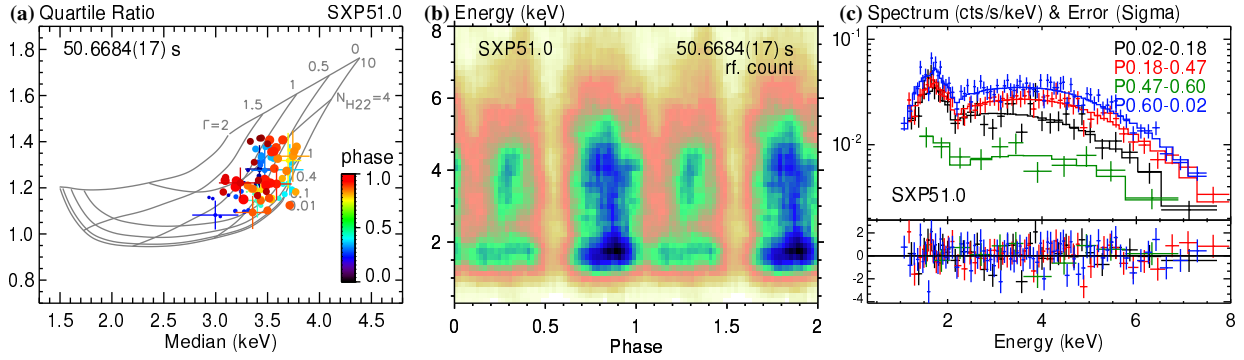


Figure 7. Phase-resolved quantile diagram, energy versus phase diagram and spectral model fits of SXP 51.0. See Section 4.3.

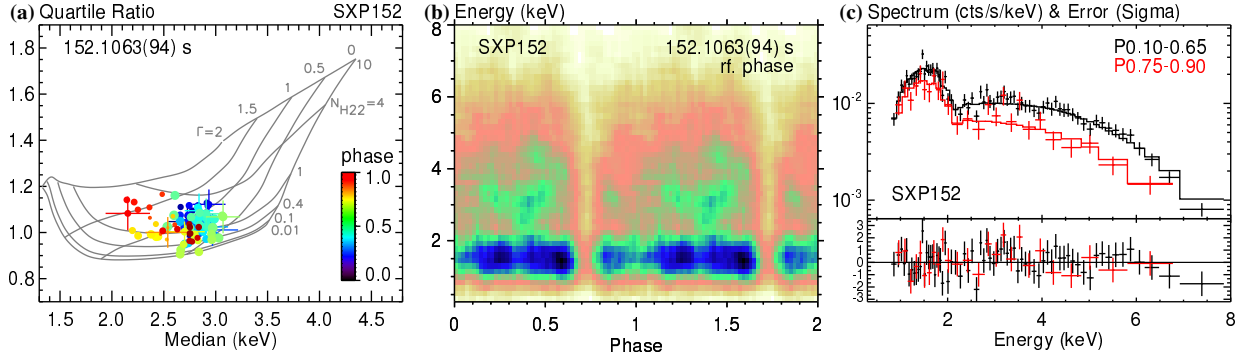


Figure 8. Phase-resolved quantile diagram, energy versus phase diagram and spectral model fits of SXP 152. See Section 4.6.

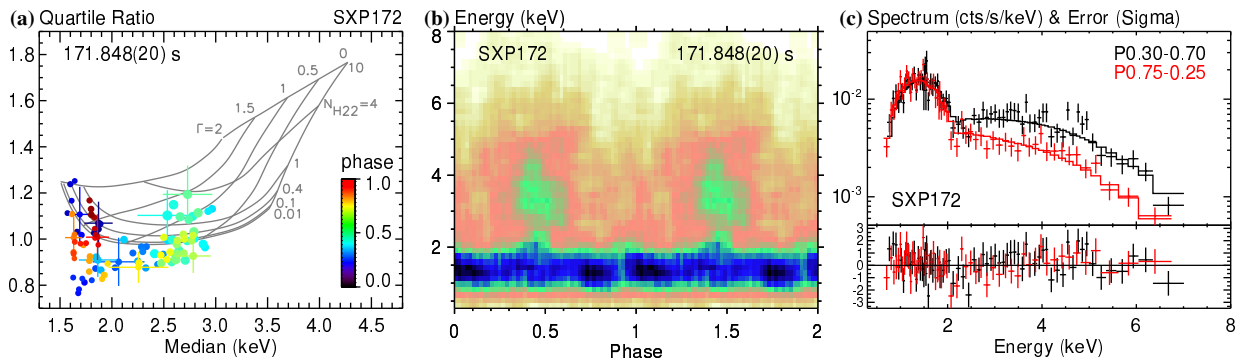


Figure 9. Phase-resolved quantile diagram, energy versus phase diagram and spectral model fits of SXP 172. See Section 4.7.

4.3. SXP 51.0

X-ray pulsations at 25.5 s from SXP 51.0 were first discovered with *RXTE* by Lamb et al. (2002a). The source was later localized as XMMU J004814.1–731003 from an *XMM-Newton* observation by Haberl et al. (2008) and has been known as SXP 25.5 for some time. It has been unclear if XMMU J004814.1–731003 is associated with AX J0048.2–7309, which is listed as SXP 51.0 in the literature. Laycock et al. (2005) showed that the 1/2nd harmonic of a period can dominate the power spectrum and claimed that the 25.5 s period is a harmonic of the 51 s period, whereas Haberl et al. (2008) failed to detect the 51 s period from the *XMM-Newton* observation.

SXP 51.0 was observed with *Chandra* in 2013 March and September. In the March observation, the source was bright with an X-ray luminosity of 1.7×10^{36} erg s $^{-1}$, which is consistent with the average luminosity observed with *RXTE* (Klus et al. 2014) within a factor of two, but in September the X-ray luminosity dropped below the 3σ detection limit of 1.4×10^{33} erg s $^{-1}$.

The elongated event distribution of the source seen in the 2013 March *Chandra* observation may suggest a possibility of two sources, but a large offset ($5.5'$) from the aimpoint is likely the origin of the wide PSF. The LS periodogram from the 2013 March *Chandra* observation shows strong pulsations at both 25.33426 ± 0.00032 s and 50.6684 ± 0.0017 s periods with ~ 25.3 s as the primary periodicity. Given the simultaneous detection of the pulsations at both periods, we believe that SXP 25.5 and SXP 51.0 are the same source.

Arumugasamy et al. (2014) argued that the spin period of PSR J2022+3842 is 48.6 ms even though they found a stronger signal at 24.3 ms in their periodogram because the folded light curve at 48.6 ms showed two distinct peaks per pulsation cycle. Similarly Mori et al. (2013) claimed the pulsation period of 3.76 s for SGR J1745–29 even though their power spectrum shows a stronger peak at 1.25 s. If we follow the same logic, the true spin period of the source is 50.6684 s since its pulse profile shows two distinct peaks with two sharp eclipse-like dips (Figure 2). On the other hand, the pulse profile folded at the primary period of 25.33426 s shows a somewhat featureless single broad peak. SXP 51.0 being misidentified as SXP 25.5 is somewhat intriguing since the apparent bimodal distribution of the spin periods among the pulsars pointed out by Knigge, Coe & Podsiadlowski (2011) is due to a paucity of pulsars with spin periods around 25 s.

The observed primary period at 25.33426 s, in fact, is significantly shorter than the spin periods reported from the previous *XMM-Newton* observations (e.g., $\gtrsim 25.45$ s in Klus et al. 2014). Figure B10 in Klus et al. (2014) shows that the source is recently on a long-term spin-up trend of $\dot{P} \sim -0.10$ s yr $^{-1}$ from MJD 55200 to 55700 (assuming $P \sim 51$ s instead of ~ 25.5 s). The spin-up trend between our measurement (MJD 56355) and the last *XMM-Newton* observation is $\dot{P} \sim -0.20$ s yr $^{-1}$, which indicates that the spin-up trend may have been accelerated.

The X-ray spectrum is well fitted by an absorbed power-law model with $\Gamma = 0.50 \pm 0.05$, which is relatively harder than $\Gamma = 1.3 \pm 0.3$ measured by Haberl et al. (2008), whereas the absorption in the spectrum

remained consistent in both measurements. The phase-resolved quantile diagram shows spectral variations with the pulsation phase as shown in Figure 7(a) & (b). The two peaks in the pulse profile exhibit a consistent spectral type with a marginal line absorption feature around 5 keV ($\sim 3\sigma$), whereas the gaps between the peaks show distinct spectral types of either being intrinsically softer or less absorbed. See Figure 7(c) and Table 6.

4.4. SXP 59.0

SXP 59.0 was first discovered as a transient pulsar in 1998 with *RXTE* by Marshall et al. (1998). Laycock et al. (2005) derived an orbital period of 123 ± 1 d from four bright X-ray bursts seen with *RXTE* in 1998 and 1999. Schmidtke & Cowley (2005) proposed an orbital period of 60.2 d from a timing analysis of the OGLE-II and MACHO data. However, Galache et al. (2008) suggested an orbital period of 122.1 ± 0.38 d based on an analysis of the *RXTE* data between 1999 September and 2002 September.

SXP 59.0 was observed with *Chandra* twice in 2006 and once in 2013. Between the 2006 and 2013 observations the X-ray luminosity decreased to 10^{34} erg s $^{-1}$ from 4×10^{34} erg s $^{-1}$ and the X-ray spectrum became intrinsically softer ($\Gamma \sim 2.6$ from 1) but more absorbed ($N_{\text{H}} \sim 6 \times 10^{22}$ cm $^{-2}$ from 10^{21} cm $^{-2}$) according to the quantile analysis. The X-ray spectrum observed in 2006 is best fitted by an absorbed power-law model with $\Gamma = 0.9 \pm 0.2$ among the four basic models but the reduced χ^2 is relatively high (1.32). The 2013 observation detected only 67 net counts from the source (Table 4).

The periodic modulation is detected in the former data set ($A_{\text{mod}} \sim 80\%$), but in the latter the low statistics limits the modulation search. The 2006 light curve shows a sudden increase in the flux (Figure 2), and the BB analysis on the compressed light curve shows three distinct blocks with the second block marking the increase in the flux.

4.5. SXP 138

Pulsations from SXP 138 were first discovered in the *Chandra* archival data by Edge et al. (2004b). Edge (2005) identified MA[93]667 as the optical counterpart and found an orbital period of ~ 125.1 d from the MACHO data. SXP 138 was observed again with *Chandra* in 2006. The LS periodogram in Figure 2 shows significant periodicities ($A_{\text{mod}} \sim 72\%$) at the spin period (138.924 ± 0.010 s) as well as the observational dithering period (1000 s) and their beating periods since the source was detected near a CCD edge. The overall light curve shows a marginal decline with an average X-ray luminosity of $\sim 2.4 \times 10^{35}$ erg s $^{-1}$ (2 BBs in Figure 2). The overall X-ray spectrum is relatively hard with $\Gamma = 0.70 \pm 0.09$ for an absorbed power-law model.

4.6. SXP 152

Pulsations from SXP 152 were first discovered from a *Chandra* observation in 2001 by Macomb et al. (2003). Our analysis covers the same data set. The LS periodogram from our analysis shows the main pulsation at 152.1063 ± 0.0094 s. The 1/2 (76.04 s) and 1/3 (50.70 s) harmonics of the main period all form significant peaks in the LS periodogram.

The folded light curve at the main period shows a sharp dip or an eclipse-like feature spanning over ~ 0.15 in phase ($A_{\text{mod}}=76\%$). This feature was used to improve the accuracy in measurement of the pulsation period (Section 3.2 and Figure 1). For instance, the pulsation period found in our analysis is consistent with 152.098 ± 0.016 s reported by Macomb et al. (2003). The event distribution in the time versus phase diagram at the latter period, however, shows that the dip in the pulse profile slips in phase with the time, similarly to the case in Figure 1(c). Therefore, we believe that our estimate of the pulsation period is more precise.

The overall spectrum is well fitted by an absorbed power-law model with $\Gamma = 0.76 \pm 0.04$. Our estimate of $N_{\text{H}} = 9 \times 10^{21} \text{ cm}^{-2}$ is higher than $5.7 \times 10^{21} \text{ cm}^{-2}$ by Macomb et al. (2003), which could be due to the different assumption of the absorption models. The observed 0.5–8 keV X-ray luminosity ($5.2 \times 10^{35} \text{ erg s}^{-1}$) is about a factor of two higher than what Macomb et al. (2003) estimated, which can be explained by the differences in the energy band (0.6–7.5 keV in the latter), the assumption for the distance to the source (57 kpc in the latter), and spectral model parameters.

The phase-resolved quantile diagram shows that the X-ray spectrum during the plateau right after the dip is intrinsically softer than the rest for an absorbed power-law model (a few red points are at $\Gamma > 1$ in the quantile diagram in Figure 8(a), see also Figure 2). Figure 8(c) and Table 7 compare the spectral model fit results of two selected phases, where a marginal spectral softening is observed after the dip. The folded light curve shows rapid fluctuations up to the ingress of the dip. Similarly to SXP 51.0, when the flux is high (phases 0.1–0.65), the X-ray spectrum of SXP 152 exhibits marginal ($\sim 3\sigma$) absorption features near 3.5 keV and 5 keV (Figure 8(c)). The absorption feature near 3.5–4 keV is identifiable in the energy versus phase diagram (Figure 8(b)) from a pocket of the lower count region near phases 0.2–0.5.

4.7. SXP 172

The X-ray pulsation from SXP 172 was first discovered by Yokogawa et al. (2000a) from three *ASCA* observations of the source in 1997, 1999, and 2000. Haberl & Pietsch (2004) confirmed the X-ray pulsations at 172.21 ± 0.13 s from an *XMM-Newton* observation in 2000. SXP 172 was observed with *Chandra* in 2006. The LS periodogram shows two significant periodicities at 171.848 ± 0.020 s and 235.831 ± 0.034 s with the latter being more significant. The source was observed near a corner of a CCD during the *Chandra* observation, but the usual dithering periods at 707 s and 1000 s are not present in the LS periodogram. The newly detected period (~ 235 s) appears to be an artifact due to a filtering between Level 1 and 2 standard CXC data products, which removed some events in the central section of the PSF. Only the Level 2 data exhibits the pulsations at ~ 235 s while the pulsations at ~ 172 s are present in both the Levels 1 and 2 data.

With an average X-ray luminosity of $3.6 \times 10^{35} \text{ erg s}^{-1}$, the overall X-ray spectrum is relatively hard with $\Gamma = 1.08 \pm 0.03$ for an absorbed power-law model. At the main 172 s period, the phase-resolved quantile diagram indicates that the high flux is correlated with an intrinsic spectral hardening (lower photon indices). Figure 9(a

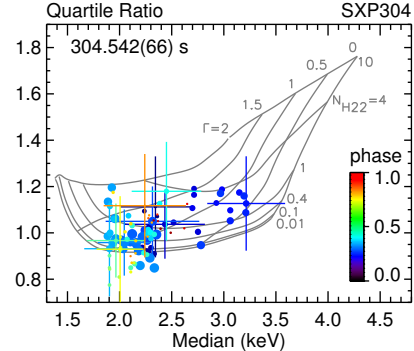


Figure 10. Phase-resolved quantile diagram of SXP 304. See Section 4.9.

and c) and Table 8 show that Γ switches between <1 and >1 during the pulsation. The energy versus phase diagram in Figure 9(b) and the multiband folded light curves in Figure 3 show that the modulation is dominated by the hard X-ray photons above 2 keV, where the hard X-ray emission peaks in phases between 0.3 and 0.7.

4.8. SXP 214

SXP 214 was discovered as a transient pulsar with a spin period of $P_s = 214$ s from an *XMM-Newton* observation in 2009 (Coe et al. 2011). The *Chandra* observation of SXP 214 in 2013 shows interesting spectral variations as a function of time (Figure 3) and the pulsation phase. Hong et al. (2016) have concluded that the NS was emerging from the circumstellar disk of the Be companion star during the *Chandra* observation. See Hong et al. (2016) for the detailed analysis and results of the *Chandra* observation of SXP 214.

4.9. SXP 304

Pulsations from SXP 304 were first discovered from a 2001 *Chandra* observation by Macomb et al. (2003). Our analysis covers the same data set. Schmidtke & Cowley (2006) estimated an orbital period of 520 ± 12 d from the MACHO data of the optical counterpart MA[93]1240.

The observed pulsation period (304.542 ± 0.066 s) is consistent with the reported value by Macomb et al. (2003). The pulse profile shows a high modulation amplitude ($A_{\text{mod}} > 80\%$) and the X-ray luminosity is the lowest ($\sim 3 \times 10^{34} \text{ erg s}^{-1}$ in 0.5–8 keV) among the sources exhibiting solid periodic modulations. Similarly to SXP 152, our spectral model fit of SXP 304 estimates a lower extinction ($N_{\text{H}} = 2 \times 10^{21} \text{ cm}^{-2}$) and a lower photon index ($\Gamma = 0.9 \pm 0.2$) than what Macomb et al. (2003) estimated. The differences in the model parameters likely contributed to our higher estimate of the X-ray luminosity (by a factor of ~ 3). The phase-resolved quantile diagram shows a marginal spectral softening ($\Gamma > 1$) associated with the flux decrease during the pulsation cycle (Figure 10).

4.10. SXP 323

Pulsations from SXP 323 were first discovered from an *ASCA* observation by Yokogawa & Koyama (1998). Cowley et al. (1997) identified a Be star as the optical counterpart. Laycock et al. (2005) suggested an orbital period of 109 ± 18 days from an early part of the *RXTE*

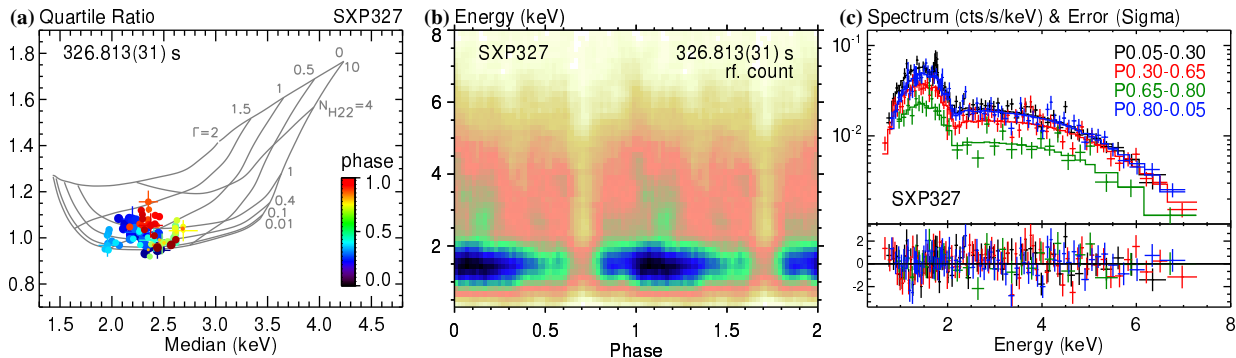


Figure 11. Phase-resolved quantile diagram, energy versus phase diagram and spectral model fits of SXP 327. See Section 4.11.

data, and Galache et al. (2008) suggested an orbital period of 116.6 ± 0.6 days from the 9 yr *RXTE* data excluding the outburst at circa MJD 52,960.

SXP 323 was observed with *Chandra* three times in 2006. The observed pulsation period (317.292 ± 0.054 s) is consistent with the overall spin-up trend seen in the *RXTE* observations (Klus et al. 2014). The pulse profile shows an eclipse-like sharp dip in phases between 0.6 and 0.7 (Figure 3). The overall X-ray spectrum is marginally fitted ($\chi_r^2 \sim 1.5$) by an absorbed power-law model with $\Gamma = 0.87 \pm 0.07$, which indicates that an additional component may be needed: the residual errors in the spectral fit show possible line absorption and emission features in the 3.5 to 4 keV band (Figure 3). The observed X-ray luminosity was about 2×10^{35} erg s $^{-1}$.

4.11. SXP 327

Pulsations from SXP 327 were first observed with *Chandra* in 2006 (Laycock et al. 2010). Udalski & Coe (2008) reported an orbital period of 45.995 d using the MACHO and OGLE-III data of the optical counterpart. The observed spin period (326.813 ± 0.031 s) is consistent with the previous result by Laycock et al. (2010). The X-ray flux of the source decreased by $\sim 10\%$ between the two observations in 2006, which were a day apart (Figure 3). The overall X-ray spectrum is fitted by an absorbed power-law model with $\Gamma = 0.90 \pm 0.03$, and the observed X-ray luminosity was about 10^{36} erg s $^{-1}$.

The pulse profile shows an eclipse-like dip in phases between 0.65 and 0.8. The phase-resolved quantile and the time versus phase diagrams show marginal but complex spectral changes during pulsation cycles (Figure 11). The spectral model fits of the segmented phases summarized in Table 9 indicate that during the dip (phases 0.65–0.8) the spectrum becomes harder ($\Gamma \sim 0.7$) with a less absorption ($N_H \sim 0$) compared to the rest of the phases ($\Gamma \geq 0.8$, $N_H \geq 10^{21}$ cm $^{-2}$).

4.12. SXP 504

Pulsations of SXP 504 were independently discovered by Edge et al. (2004a) from the *Chandra* archival data and by Haberl & Pietsch (2004) from an *XMM-Newton* observation. Edge et al. (2004a) reported a period of 268.6 ± 0.1 d in the MACHO and OGLE-II data of the optical counterpart.

SXP 504 was observed again with *Chandra* twice, five months apart, in 2013. In both observations, the source

was detected near a CCD edge and the modulation period is close to the 1/2 harmonics of the known 1000 s dithering period, but there was no sign of periodic modulations at 1000 s. Both observations show a strong modulation at ~ 501.3 sec, which is consistent with the periods observed in the past (Klus et al. 2014). The overall X-ray luminosity increased by about 60% between the two observations in 2013 (from 3.9×10^{34} to 6.1×10^{34} erg s $^{-1}$, Figure 3 and Table 4).

The X-ray spectrum of the first observation is well fitted with an absorbed power-law, thermal bremsstrahlung, and APEC models, whereas the second observation shows a good spectral fit only with an absorbed power-law model, the X-ray spectra show similar photon indices ($\Gamma = 0.8 \pm 0.1$, 0.60 ± 0.08) between the two observations whereas the absorption had dropped from $N_H = 1.3 \times 10^{22}$ to 3×10^{21} cm $^{-2}$, which may explain the increase in the observed X-ray luminosity of the second observation. The pulse profiles also show minor changes between the two observations, exhibiting more features (e.g., a sharp rise at a phase around 0.6) and a larger modulation amplitude (from 65% to 79%) in the second observation (Figure 3 and Table 3).

4.13. SXP 565

Pulsations from SXP 565 were first discovered from the 2001 *Chandra* observation by Macomb et al. (2003). Schmidtke et al. (2004) reported a period of 95.3 d from the optical counterpart, while Edge (2005) did not detect this period from the early OGLE data. Galache et al. (2008) reported a period of 151.8 d from the *RXTE* observations, and Rajoelimanana et al. (2011) measured a period of 152.4 d from the OGLE-III data, suggesting that the 152.4 d period is the orbital period of SXP 565.

SXP 565 was observed again with *Chandra* in 2013 March and September. The observed X-ray luminosity has increased to $\sim 2.4 \times 10^{34}$ erg s $^{-1}$ in the 2013 observation from $\sim 1.9 \times 10^{34}$ erg s $^{-1}$ in 2001. The pulsation, however, was only detected in the 2001 observation although it was observed far off-axis in the ACIS S3 chip (11' from the aimpoint). The upper limit of the modulation amplitude is about 27% in the 2013 observations, while the observed modulation amplitude in the 2001 observation is about 67%.

The X-ray spectrum became a bit harder in 2013 compared to 2001. For an absorbed power-law model, the absorption increased ($N_H = 1.0 \times 10^{22}$ to 2.8×10^{22} cm $^{-2}$)

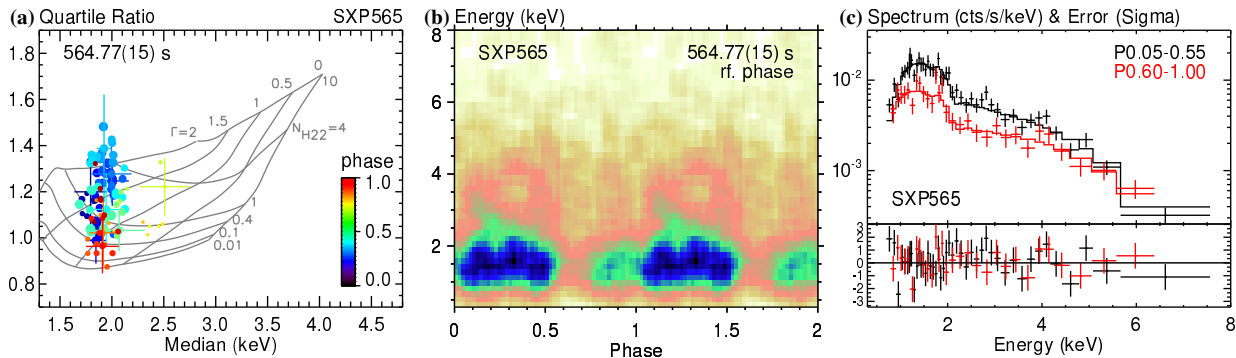


Figure 12. Phase-resolved quantile diagram, energy versus phase diagram and spectral model fits of SXP 565. See Section 4.13.

while the photon index remained constant ($\Gamma = 1.16 \pm 0.07$ to 1.07 ± 0.09 , Table 4). The pulse profile shows step-wise rises at phases ~ 0.8 and 0.1 from the minimum to maximum (Figure 4). The phase-resolved quantile and the energy versus phase diagrams in Figure 12 show a complex variation of the absorption, the photon index, and the flux during the pulsation. The spectral fits of the high and low state phases in Figure 12 and Table 10 show that the X-ray spectrum during the high flux phases (0.05–0.55) is softer ($\Gamma \sim 1.3$ versus 0.8) but more absorbed ($N_{\text{H}} \sim 1.4 \times 10^{22}$ versus $5 \times 10^{21} \text{ cm}^{-2}$) than the spectrum of the rest.

4.14. SXP 701

Pulsations from SXP 701 were first discovered from an *XMM-Newton* observation by Haberl et al. (2004b, 2004c). Schmidtke & Cowley (2005) and Rajoelimanana et al. (2011) found a 412 d period from the MACHO and OGLE-III data of the optical counterpart, respectively.

SXP 701 was observed with *Chandra* in 2013 January and June. The X-ray luminosity has dropped roughly by half between the two observations from $2.2 \times 10^{35} \text{ erg s}^{-1}$ to $10^{35} \text{ erg s}^{-1}$ (Table 4). The X-ray spectra of the two observations are well fitted by an absorbed power-law model. Both the photon index ($\Gamma \sim 0.9 - 1.0$) and the absorption ($N_{\text{H}} \sim 2 \times 10^{21} \text{ cm}^{-2}$) have remained more or less constant between the two observations.

The source showed a strong pulsation at $726.31 \pm 0.44 \text{ s}$ and $728.11 \pm 0.57 \text{ s}$ in the 2013 January and June observations, respectively. As shown in Figure 13(a), these periods are not consistent with the periods observed in the past (Klus et al. 2014), which show essentially no long-term change ($\dot{P} \sim 0.0 \pm 0.3 \text{ s yr}^{-1}$, $P_s \sim 691\text{--}703 \text{ s}$). The pulsar appears to be experiencing a rapid spin-down trend ($\dot{P} \sim +3.8 \text{ s yr}^{-1}$) between the two *Chandra* observations. When comparing with the mean period ($P_s \sim 699 \text{ s}$) or the last data point ($P_s \sim 691 \text{ s}$ at $\sim \text{MJD } 55650$) of the *RXTE* measurements reported by Klus et al. (2014), the change appears even more extreme with $\dot{P}_s \sim +15 - 20 \text{ s yr}^{-1}$.

In terms of the characteristic spin-down timescale ($\tau_{\text{sd}} = P/2\dot{P}$), the observed change in the spin period is remarkable: $\tau_{\text{sd}} \sim 20\text{--}100 \text{ yr}$. For comparison, 4U 2206+54, which is an HMXB with a slowly spinning pulsar in a rapid spin-down trend ($P_s \sim 5555 \text{ s}$, $\dot{P}_s \sim 16 \text{ s yr}^{-1}$) shows $\tau_{\text{sd}} \sim 180 \text{ yr}$ (Wang & Chang 2012; Ikhsanov & Beskrovnaya 2013). According to the long-term spin

trends of the SMC pulsars discussed by Klus et al. (2014), only three pulsars (SXP 74.7, SXP 91.1, and SXP 342) show a larger relative change in their spin periods over the 15 year monitoring using *RXTE*, but their spin periods are much shorter than SXP 701. SXP 756 and SXP 1323, which may be similar to SXP 701 in terms of the binary parameters, have been exhibiting large chaotic changes in their spin periods. However, what is unique about SXP 701 is its spin period has been somewhat stable until our survey. Therefore, the recent change in the spin period of SXP 701 may provide a new clue to the origin of the slowly spinning pulsars.

Fig. 13(b) illustrates the relationship between the X-ray luminosities and the spin periods of SXP 701. According to Shakura et al. (2012), who showed that a quasi-spherical subsonic accretion flow can slow down the NS without the need for a high surface magnetic field, a subsonic settling can be realized at relatively low X-ray luminosities (i.e., low accretion rate), $L_X < 4 \times 10^{36} \text{ erg s}^{-1}$. While the precise threshold of the X-ray luminosity for the transition may vary for each system, Fig. 13(b) suggests that SXP 701 may have undergone a similar transition at $\sim 3 \times 10^{35} \text{ erg s}^{-1}$. This is reminiscent of torque reversals observed in the wind-fed pulsars like Vela X-1, GX 301-2, and GX 1+4, but the precise distance information of the SMC pulsars allows an accurate determination of the threshold luminosity, if any, (and thus the corresponding accretion rate) for the transition. In fact, the suggested transition luminosity of SXP 701 is similar to the turn over at $\sim 4 \times 10^{35} \text{ erg s}^{-1}$ in the X-ray luminosity function of the SMC HMXBs (Antoniou et al. 2017 in preparation). This implies that the spin-down trend of SXP 701 may have been triggered by or related to the propeller effect (the centrifugal inhibition of accretion due to the pulsar’s magnetic field Illarionov & Sunyaev 1975), perhaps suggesting yet another path to slowly spinning pulsars.

4.15. SXP 756

SXP 756 was discovered as the slowest X-ray pulsar at the time by Yokogawa et al. (2000b) from *ASCA* observations. Laycock et al. (2005) reported an X-ray period of 396 d, and Cowley & Schmidtke (2003) and Schmidtke et al. (2004) reported recurring optical outbursts at $\sim 394 \text{ d}$ intervals from the MACHO data of the counterpart. Galache et al. (2008) found an orbital period of $389.9 \pm 7.0 \text{ d}$ from the *RXTE* data.

SXP 756 was observed with *Chandra* in 2006. The

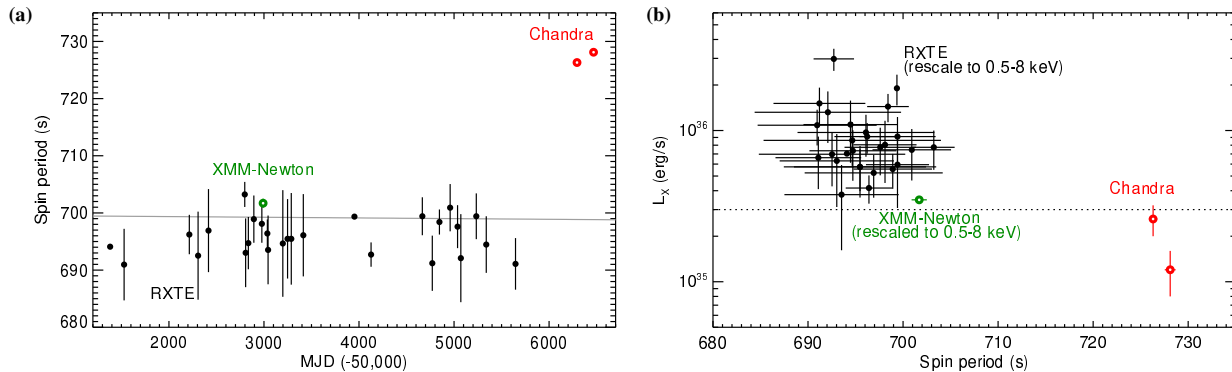


Figure 13. (a) Spin period evolution of SXP 701. The *RXTE* measurements (black) and the long-term trend (the grey line) are from (Klus et al. 2014). The *XMM-Newton* (green) and *Chandra* (red) measurements are from Haberl et al. (2004c) and this analysis, respectively. (b) The intrinsic 0.5–8 keV X-ray luminosity (L_X) versus the spin period of SXP 701. The X-ray luminosities from *RXTE* and *XMM-Newton* are rescaled to the 0.5–8 keV band for an absorbed power-law model with $\Gamma=1$ and $N_H = 2 \times 10^{22} \text{ cm}^{-2}$ (and also with a 60% pulsed fraction for *RXTE*; see Eq. (1) in (Klus et al. 2014)).

pulsation period is found at $746.43 \pm 0.22 \text{ s}$, which agrees with the previous report by Laycock et al. (2010) from the same data set. The 1/2 harmonic of the period also forms a significant peak in the LS periodogram. The X-ray spectrum is well fitted by an absorbed power-law model with $\Gamma = 0.76 \pm 0.05$ and $N_H = 1.1 \times 10^{22} \text{ cm}^{-2}$. The observed X-ray luminosity is $4.7 \times 10^{34} \text{ erg s}^{-1}$ at 60 kpc. The X-ray count rate in Figure 4 shows a slight increase during the observations.

The phase-resolved quantile diagram in Figure 14(a) reveals the spectral variations correlated with the pulsation cycle. The energy versus phase diagram in Figure 14(b) as well as the multiband folded light curves in Figure 4 indicate separate minimum phases for soft and hard X-rays: at phases ~ 0.7 below 2 keV and at phases ~ 0.2 above 2 keV. The phase-resolved spectral fits in Figure 14(c) and Table 11 show that the high flux phase (0.45–0.70) exhibits a heavier absorption by a factor of 2 while the photon index remains constant ($\Gamma \sim 0.8$).

4.16. SXP 893

Pulsations from SXP 893 were first discovered from a 2001 *Chandra* observation by Laycock et al. (2010). Since then, SXP 893 was observed again with *Chandra* in 2013 March and September. The periodic X-ray modulations are detected in the 2001 November and 2013 September observations with $A_{\text{mod}} \gtrsim 80\%$. The 2013 March observation, when the X-ray count rate dropped by a factor of > 2 compared to the other observations, does not show any significant periodic modulation ($A_{\text{mod}} < 41\%$). The measured periods are within the normal range of the spin periods observed with *RXTE* by Klus et al. (2014). The pulse profile from the 2001 observation shows an eclipse-like dip at phase ~ 0.2 , and the 2013 pulse profile shows a similar dip in the flux at phase ~ 0.5 (Figure 4), but note the different definition of phase 0.

The X-ray luminosity almost doubled between the 2001 November and 2013 September observations (from 1.7×10^{35} to $2.9 \times 10^{35} \text{ erg s}^{-1}$, Table 4). Note that our estimate of the X-ray luminosity during the 2001 observation is 80% higher than the estimate by Laycock et al. (2010). The difference is due to the different assumptions of the spectral models and parameters. The X-ray spectra are well fitted by an absorbed power-law model.

While the photon index remained more or less constant ($\Gamma \sim 0.6$ – 0.7) between the two observations, the absorption N_H dropped by more than half from 1.6×10^{22} to $7 \times 10^{21} \text{ cm}^{-2}$ (albeit with large uncertainties).

4.17. SXP 5.05

SXP 5.05 was first discovered as a transient X-ray source with *INTEGRAL* by Coe et al. (2013a). Designated as IGR J00569–7226, it is a relatively new addition among the SMC pulsars described in this paper. Its pulsation was first discovered in a combination of *Swift* and *XMM-Newton* observations by Coe et al. (2013b). Coe et al. (2015) determined the orbital parameters with a binary period of $17.13 \pm 0.14 \text{ d}$ through the measurement of the changes in the spin periods from multiple *Swift* observations. They also argued that the NS is viewed through the circumstellar disk periodically during orbital motions, which leads to the observed flux variation aligned with the orbital period.

SXP 5.05 was observed with *Chandra* in 2001 January and 2013 January, June and September. Only in the last observation the source was detected with a high count rate reaching $0.8 \text{ counts s}^{-1}$. The source was observed at $6.4'$ off the aimpoint with *Chandra*, so there is no or little pile-up in the *Chandra* data. The upper limit (3σ) of the X-ray luminosity during the early observations with no detection ranges from 2.3 to $4.7 \times 10^{33} \text{ erg s}^{-1}$ at 60 kpc.

The pulsation period of SXP 5.05 is too short to be detected with the *Chandra* ACIS chips using the LS periodogram, given the $\sim 3.14 \text{ s}$ readout cycle. The EF periodogram of the last observation, albeit noisy, shows a sharp peak at $5.05019 \pm 0.00013 \text{ s}$ (Figure 15), but it is likely due to phase aliasing between the pulsation period and the CCD readout cycle because (1) the pulse profile folded at 5.05019 s rapidly fluctuates between the minimum and maximum during a pulsation cycle and (2) the periodogram, which is generated from the randomized time tags of X-ray events within each readout cycle, does not exhibit sharp peaks (light blue curves in Figure 15).

The LS periodogram shows additional marginal periodicities at $958.0 \pm 1.4 \text{ s}$ and $3018 \pm 13 \text{ s}$ (Figure 5). While the origin of these periods is not clear, the light curve of the 2013 September observation in Figure 5 ex-

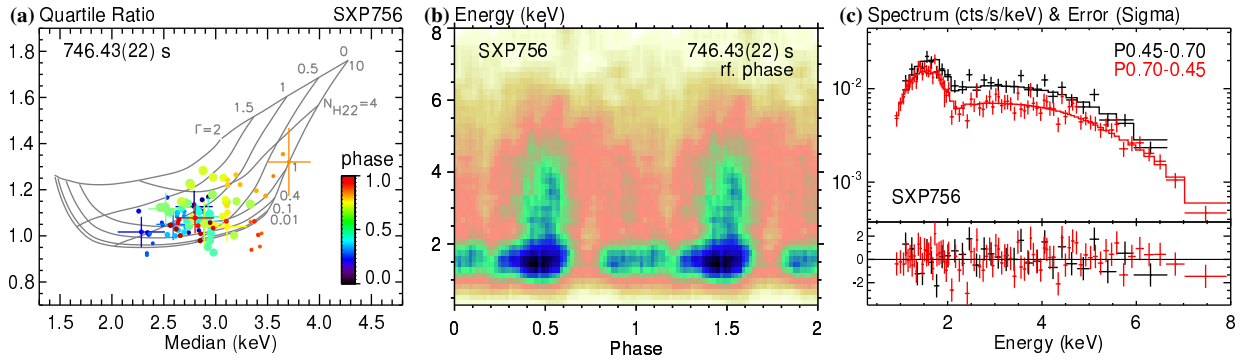


Figure 14. Phase-resolved quantile diagram, energy versus phase diagram and spectral model fits of SXP 756. See Section 4.15.

hibits several oscillations at ~ 8 – 10 ks period (4 BBs in Obs. ID 15504).

The *Chandra* light curve also shows an overall decrease in the count rate from 800 to 600 counts per ks, indicating that the observation may have caught a part of the long-term decline from an outburst in 2013 (Coe et al. 2015). On the other hand, the *XMM-Newton* observations of SXP 5.05 in 2013 November and December show $L_X > 10^{37}$ erg s^{-1} (Coe et al. 2015), which is higher than $L_X \sim 9.1 \times 10^{36}$ erg s^{-1} measured with *Chandra* in 2013 September, implying possible multiple outbursts from the source. The *Chandra* X-ray spectrum is well fitted by an absorbed power-law model with $\Gamma = 0.17 \pm 0.01$.

4.18. *CXOU J003942.37-732427.4* or SXP 7.59?

CXOU J003942.37-732427.4 is a new candidate pulsar with a marginal detection (82.5% confidence) of the pulsation at 7.58712 ± 0.00012 s from the 2013 *Chandra* observation ($A_{\text{mod}} = 58\%$). The source was observed again with *Chandra* in 2014 when its X-ray luminosity increased to 7×10^{34} erg s^{-1} from 3×10^{34} erg s^{-1} in 2013. The X-ray count rates also doubled between the two observations (Table 4), but the 2014 observation does not show any periodicity ($A_{\text{mod}} < 65\%$). Given the small number of total net counts (151) detected in the 2013 observation, further observations in future will be needed to confirm the pulsation of the source. Also note that there is no proper counterpart for an HMXB at the *Chandra* position: the nearest possible counterpart is an AGN (Kozłowski et al. 2013). The lack of early-type star in the error circle of the *Chandra* position suggests that if it is a pulsar, it is not in an HXMB system.

According to the quantile analysis (Table 4), the X-ray spectrum softened between the two observations due to an apparent reduction in the absorption from $N_H \sim 7 \times 10^{22}$ cm^{-2} to 2×10^{22} cm^{-2} with a constant photon index of $\Gamma \sim 1.2$ for an absorbed power-law model. The reduction in the absorption partially explains the increase in the observed X-ray luminosities between the two observations.

4.19. SXP 8.02

SXP 8.02 is the only known magnetar in the SMC. Lamb et al. (2002b) first suggested that SXP 8.02 is an anomalous X-ray pulsar (AXP) based on the detection of X-ray pulsations from the 2001 *Chandra* observation. The fast Fourier transform (FFT) analysis by Lamb et al.

(2002b) showed roughly the equal power from the 5.4 and 8.02 s periods. Our LS periodogram shows that the main period at 8.018944 ± 0.000058 s has a much stronger power ($X \sim 18$) than the 5.43988 s period ($X \sim 12$). Unlike the double peak profile seen in the *XMM-Newton* observations (Tiengo et al. 2008), the *Chandra* pulse profile shows a single broad peak over each pulsation cycle (Figure 5), which could be in part due to phase mixing from the 3.24 s CCD readout cycle.

The X-ray spectrum of SXP 8.02 is the softest among the pulsars in this survey and softer than the majority of the SMC field X-ray sources (see Section 5). It cannot be fitted by any of the four basic spectral models considered here: e.g., Lamb et al. (2002b) got $\chi_r^2 \sim 1.4$ for an absorbed blackbody model. Instead, it is better fitted ($\chi_r^2 \sim 1.15$) by an absorbed two-temperature blackbody model with kT s of 0.39 ± 0.06 and 3.7 ± 0.6 keV. The X-ray spectrum is consistent with those reported by Tiengo et al. (2008) from the *XMM-Newton* observations. Tiengo et al. (2008) constrained the NS radius at 12.5 km using a two-temperature blackbody model. The 0.5–8 keV X-ray luminosity is estimated to be 2.0×10^{35} erg s^{-1} , which is somewhat higher than 1.3×10^{35} erg s^{-1} by Lamb et al. (2002b). The difference is likely due to the different assumptions of the spectral model.

4.20. SXP 74.7

X-ray pulsations from SXP 74.7 were first discovered with *RXTE* by Yokogawa & Koyama (1998). Schmidtke & Cowley (2005) reported an orbital period of 33.4 ± 0.4 d in the MACHO light curve, and more recently Rajoelimanana et al. (2011) reported a period of 33.38 ± 0.01 d in the detrended light curve generated from the MACHO and OGLE observations.

SXP 74.7 was observed with *Chandra* in 2013 and 2014. The X-ray luminosity decreased from 1.7×10^{35} erg s^{-1} to 3.0×10^{34} erg s^{-1} between the two observations. The X-ray spectrum is well fitted by an absorbed power-law model with $\Gamma \sim 1$ and no significant spectral change is observed between the two observations.

The LS periodogram in Figure 5 shows a marginal periodicity at 24.9452 ± 0.0012 s, but not at the reported pulsation period of ~ 74.7 s. On the other hand, the EF periodograms in Figure 16 show similarly significant peaks at both 24.9452 and 74.836 s. The folded light curves show a single broad peak for the 24.9452 s period and three distinct peaks for 74.836 s, which indicates that the latter is the true spin period (similarly to SXP 51.0;

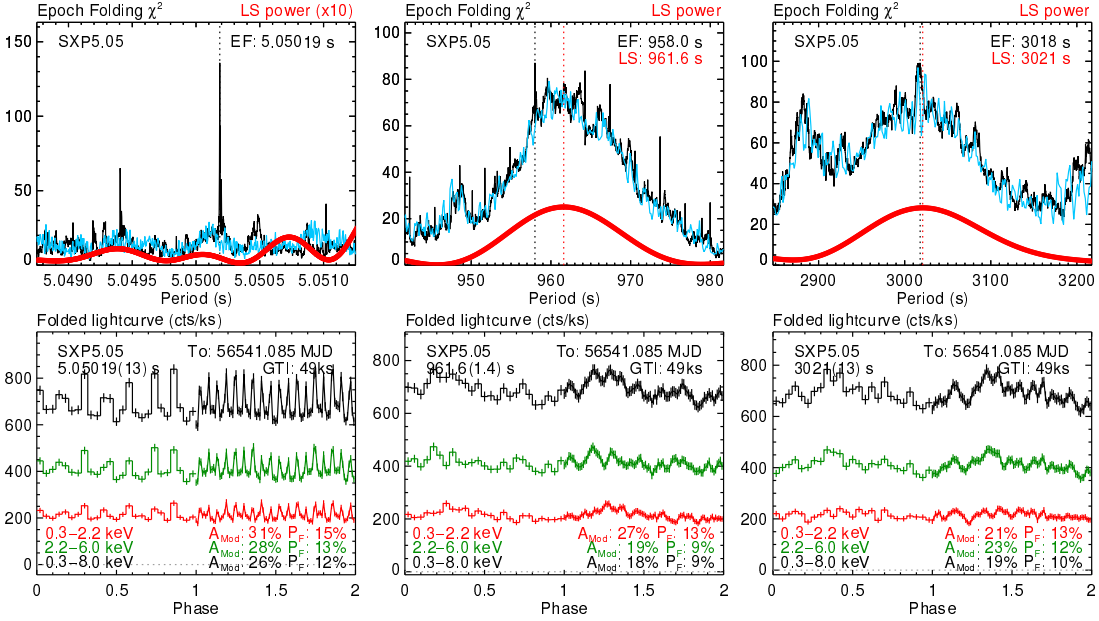


Figure 15. EF and LS periodograms (*top panels*) and corresponding folded light curves (*bottom panels*) in the 0.3–2.2, 2.2–6.0, and 0.3–8.0 keV bands of SXP 5.05 at around 5.05 s (*left*), 958 s (*middle*) and 3018 s (*right*) periods. The folded light curve at 5.05019 s is choppy due to phase mixing and aliasing from the similar CCD readout cycle (3.14 s). The light blue lines indicate the EF periodogram using the time series randomized within each readout cycle. The EF folding periodogram is noisy near the 3018 s period, which is likely related to the long-term variation seen in the unfolded light curve in Figure 5. See Section 4.17.

see Section 4.3).

The phase-resolved spectral analysis in Figure 16 shows a marginal spectral variation during pulsation: the X-ray spectrum gets intrinsically harder with $\Gamma \sim 2, 1.5$, and 1 at the first, second and third peaks, respectively.

4.21. CXOU J005446.38–722523.0 or SXP 4693?

CXOU J005446.3–722523 was observed with *Chandra* in 2006 and 2013. The source was detected in 2006, but not in 2013. The observed X-ray luminosity was 1.2×10^{34} erg s $^{-1}$ at 60 kpc and the upper limit (3σ) during the 2013 observation was 2×10^{33} erg s $^{-1}$. The X-ray spectrum is consistent with an absorbed power-law model of $\Gamma \sim 2$ according to a quantile analysis.

The 2006 observation of the source shows a very long pulsation period at 4693 ± 20 s (Laycock et al. 2010). Our analysis also shows a marginal detection of the long pulsation at 4685 ± 23 s based on the refined search using the LS periodogram. Given the increase in the period search trials in this analysis compared to Laycock et al. (2010), now the LS power of the observed period corresponds to only about 50% confidence under the assumption of a blind survey. Note that the total net counts of the source is only 151.

Intriguing is the fact that CXOU J005446.3–722523 is about 2'' off the reported optical counterpart of SXP 6.88 (Coe & Kirk 2015). The EF periodogram of CXOU J005446.3–722523 around 6.88 s does not show any clear sign of periodicity above the noise distribution. Since SXP 6.88 is an *INTEGRAL* source with a relatively large positional uncertainty of the X-ray source (McBride et al. 2007), it is not clear that the observed long pulsation from CXOU J005446.3–722523 is actually from SXP 6.88. There is also indication for the long period in *XMM-Newton* data and no indication for 6.88 s (Haberl

& Sturm 2016).

While additional observations of CXOU J005446.3–722523 are needed to validate the observed long spin period, the origin of the slowly spinning pulsars have been challenging to the conventional formation and evolutionary theory of pulsars, where long spin periods ($P_s \gtrsim 500$ s) are associated with extremely high magnetic field ($\gtrsim 10^{13}$ G) on the surface of the pulsar (e.g., Ghosh & Lamb 1979; Kluźniak & Rappaport 2007). For instance, Finger et al. (2010) interpreted 4U 2206+54 ($P_s \sim 5560$ s) as an accreting magnetar. Efforts to explain the long period pulsars by alternative models are accumulating: Ikhsanov (2007) incorporated a subsonic propeller state into the evolutionary tracks of NSs, which can overcome the spin period barrier of ~ 500 s; Wang & Chang (2012) proposed a retrograde wind accretion to explain long spin periods of supergiant fast X-ray transients (see also Christodoulou et al. 2017); Ikhsanov & Beskrovnaya (2013) suggested a magnetized accretion stream to explain the long spin period of 4U 2206+54 where the magnetic field at the surface of the NS is expected to be $\sim 4 \times 10^{12}$ G; Shakura et al. (2012, 2013) developed a model for quasi-spherical subsonic accretion, which can explain long spin periods of the NSs in symbiotic XRBs.

5. DISCUSSION

We have analyzed the deep *Chandra* survey of the SMC in search for X-ray pulsars. The LS and EF analysis showed that 21 sources including a new candidate pulsar (CXOU J003942.37–732427.4) exhibited X-ray pulsations. We have also detected another 12 known pulsars with no X-ray pulsations, six of which, though, were detected only with less than 100 net counts, and thus were too faint for pulsation search. Laycock et al. (2010) claimed pulsation detections from SXP 8.88

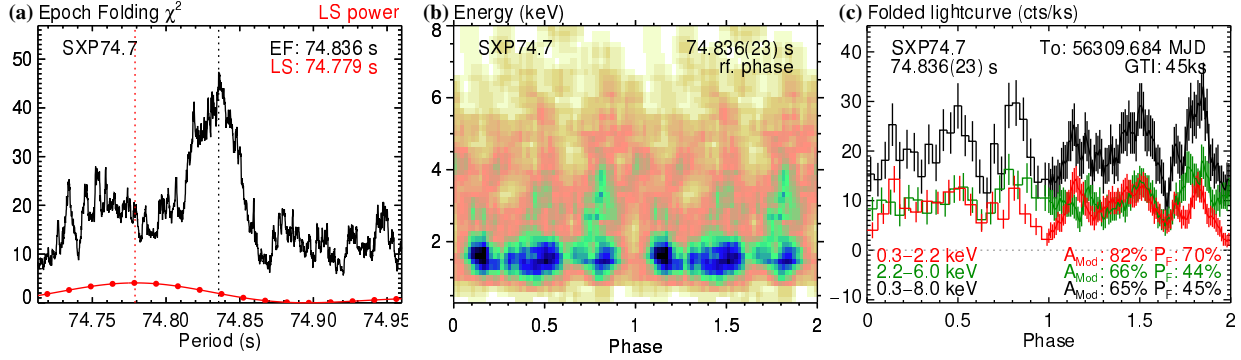


Figure 16. LS and EF periodograms, energy versus phase diagram, folded light curves (*right-middle*) of SXP 74.7 at the 74.836 s period. See Section 4.20.

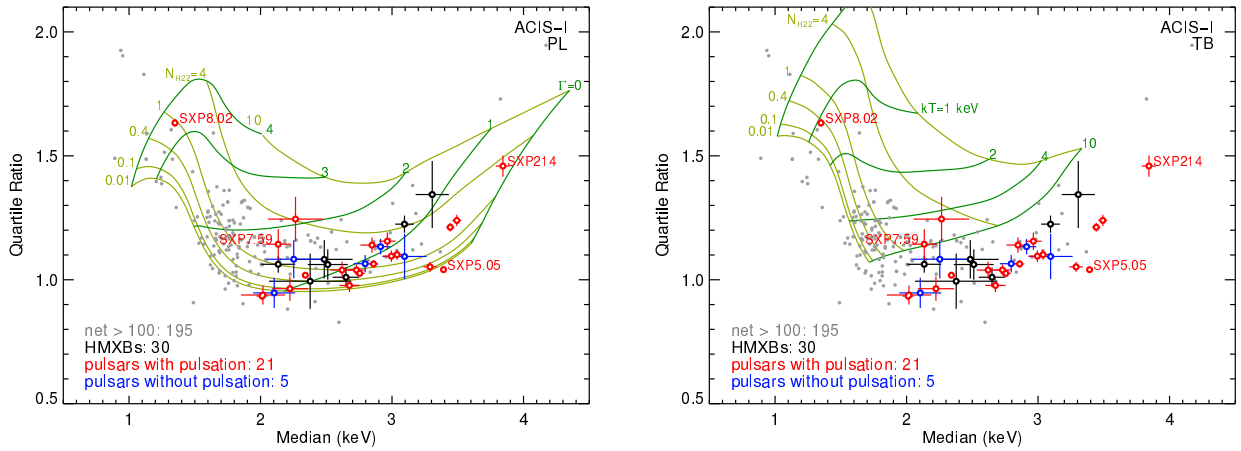


Figure 17. Quantile diagram of the SMC pulsars (red and blue) and HMXBs (black) in comparison with the SMC field sources (grey) with ≥ 100 net counts in 0.3–8 keV. Only the sources detected in the ACIS-I chips are shown. Absorbed power-law (*left*) and thermal bremsstrahlung (*right*) models are shown in grids for comparison. The grids cover the SMC local absorption with $N_{\text{H}} = 0.01, 0.1, 0.4, 1, 4, \text{ and } 10 \times 10^{22} \text{ cm}^{-2}$. In the power-law models, the grids cover $\Gamma = 0, 1, 2, 3, \text{ and } 4$. In the thermal bremsstrahlung models, the grids show the plasma temperature $kT = 0.4, 1, 2, 4, \text{ and } 10 \text{ keV}$.

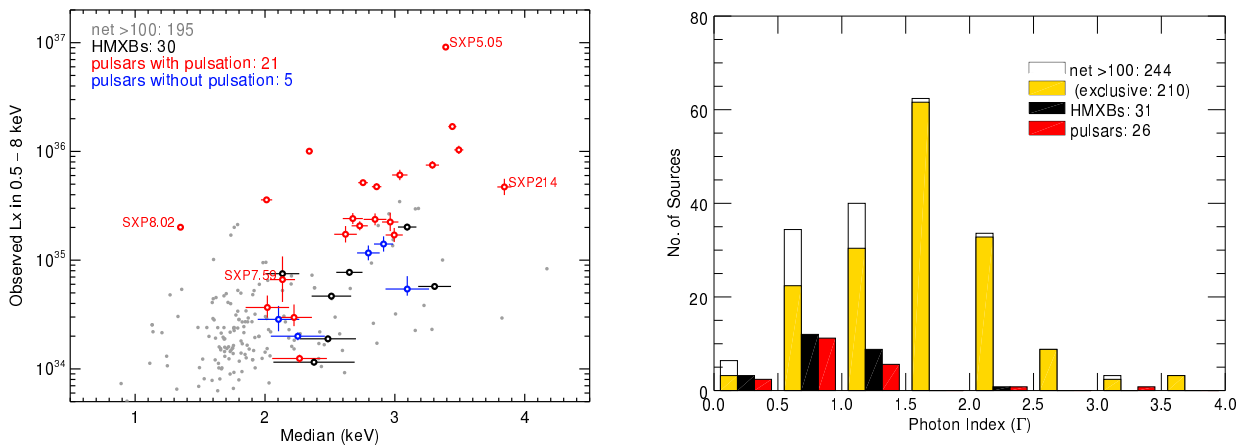


Figure 18. Observed X-ray luminosity in 0.5–8 keV at 60 kpc versus the median energy of the SMC field sources, HMXBs, and pulsars (*left*, only from the ACIS-I chips) shown in Figure 17. Distribution of the photon indices for the absorbed power-law models (*right*, from both the ACIS-I and S chips). The X-ray spectra of the SMC HMXBs and pulsars are in general harder than those of the SMC field sources.

and SXP 15.3, but the claimed peaks of their LS periodograms are well below the detection threshold set in this analysis, so we do not include them in the list of the pulsation detections. It is possible that another four pulsars (SXP 4.78, SXP 6.88, SXP 16.6, and SXP 95.2) were in the FoV of the *Chandra* observations. SXP 6.88 could be the same source as SXP 4693 (Section 4.21). The X-ray positions of the other three sources are too uncertain to conclusively associate or rule out any association with *Chandra* sources.

Here we review the collective X-ray timing and spectral properties of SMC pulsars, and compare them with those of HMXBs without pulsations and the field sources in the SMC. See also (Yang et al. 2017).

5.1. X-ray properties of SMC pulsars and field sources

Figure 17 compares the energy quantiles of the SMC field sources with the pulsars and HMXBs for absorbed power-law and thermal bremsstrahlung models. The sources with at least 100 net counts are plotted to limit the statistical uncertainty. Only the sources detected in the ACIS-I chips are shown for a proper comparison with the spectral model grids since the grid pattern depends on the detector response. The spectral models assume two absorption components: the fixed Galactic foreground and variable SMC local components (Section 4), where the latter is parameterized in the grid pattern along with the photon indices for the power-law models and the plasma temperatures for the thermal bremsstrahlung models. All the pulsars but the new candidate (CXOU J003942.37–732427.4) and the magnetar SXP 8.02 are identified as HMXBs as well. Excluding the magnetar, the pulsars and the HMXBs exhibit intrinsically harder X-ray spectra (median energy $\gtrsim 2$ keV) than the SMC field sources. For the thermal bremsstrahlung models, the plasma temperatures of $> 90\%$ of pulsars and HMXBs are above 10 keV.

Figure 18 shows the observed X-ray luminosities versus the median energy of the X-ray spectra. All the *Chandra* sources with $L_X \gtrsim 4 \times 10^{35}$ erg s $^{-1}$ exhibit X-ray pulsations, and more luminous pulsars show harder spectra. The majority of the field sources are at luminosities below 10^{35} erg s $^{-1}$, many of which have the median energy below 2 keV unlike the HMXBs and pulsars. Figure 18 also shows the distribution of the photon indices: the field source distribution peaks at $\Gamma = 1.5$ –2.0, whereas the distributions of the SMC HMXBs and pulsars peak at $\Gamma = 0.5$ –1.0. The observed photon indices of the SMC pulsars are in excellent agreement with typical spectra of pulsars. The hard X-ray spectra of HMXBs without known pulsation reinforce the notion that they are likely associated with accreting pulsars.

5.2. Spin periods, pulsed fraction and X-ray luminosities

Figure 19 shows the relations among the spin periods, the pulsed fractions, and the observed 0.5–8 keV X-ray luminosities (during the pulsations) of the SXPs in our survey. There appears to be no clear correlation among these observables. The pulsed fractions and spin periods show a marginal correlation, but the relatively low pulsed fraction at spin periods shorter than 10 s could be in part due to the relatively long CCD readout cycle. SXP 5.05 is excluded in Figure 19 since its pulsed

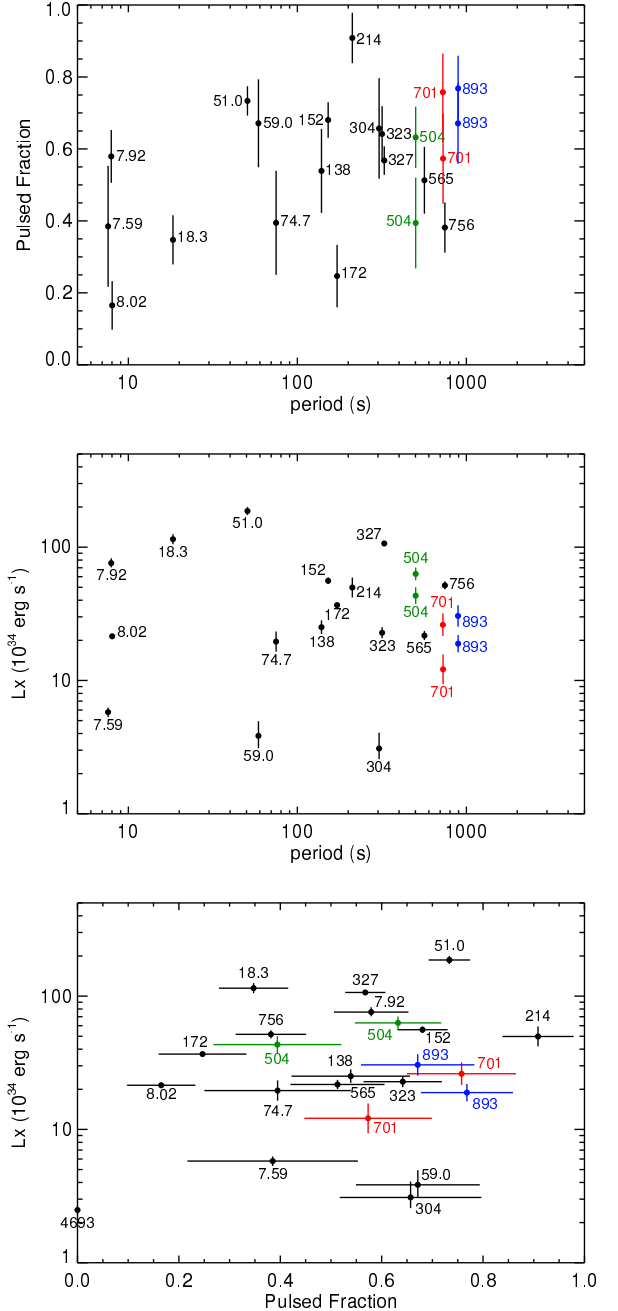


Figure 19. Relations among the spin periods, the pulsed fractions, and the observed 0.5–8 keV X-ray luminosities of the SMC pulsars (excluding SXP 5.05). For SXP 504 (green), SXP 701 (red), and SXP 893 (blue), the results of two measurements per each are shown.

fraction at the primary period is not reliably measured for its spin period due to the CCD readout time being similar to the spin period.

5.3. Unusual spin periods

Klus et al. (2014) reported the long-term trend of the spin periods of 42 SMC pulsars using the 15 yr *RXTE* data from 1997 to 2012. They found that 26 and 15 pulsars show spin-up and spin-down trends, respectively, and one pulsar (SXP 701) shows no change on average. Overall the average rate change of the spin periods is

small with \dot{P}/P ranging from $-5 \times 10^{-3} \text{ yr}^{-1}$ to $3 \times 10^{-3} \text{ yr}^{-1}$, suggesting that many of them might have achieved spin equilibrium. On the other hand, the NSs in high eccentric orbits of Be-XRB systems can go through a periodic accretion phase, which can lead to a sudden change in the spin period.

In our analysis, three pulsars (SXP 51.0, SXP 214 and SXP 701) show a large deviation in their spin periods compared to their previously reported values or long-term trends. The eccentricities of these pulsars are not known. The recent spin-up trend of SXP 214 could be as high as $-\dot{P}/P \sim 8 \times 10^{-3} \text{ yr}^{-1}$. See Hong et al. (2016) for the details. In the case of SXP 51.0, its spin-up trend appears to have doubled recently ($-\dot{P}/P \sim 4 \times 10^{-3} \text{ yr}^{-1}$, Section 4.3). SXP 701 shows the most dramatic change in the spin period with a rapid spin-down trend of $\dot{P}/P \sim 5.4 \times 10^{-3} \text{ yr}^{-1}$ to $\sim 2 \times 10^{-2} \text{ yr}^{-1}$, breaking from a spin-equilibrium state of likely more than 15 yrs (Section 4.14). If the recent change is more permanent than chaotic, SXP 701 may provide a unique insight to the physics behind the formation of slowly spinning pulsars. Given the unusual rapid change in recent years, further monitoring of these sources is needed to understand the cause of the spin change trend.

5.4. Eclipse-like dips in pulse profiles

The relatively low background in the *Chandra* observations due to the superb angular resolution of the *Chandra* X-ray optics enables measurements of precise pulsation profiles, which can be used for modeling the geometry of the NS and the pulsated X-ray emissions. Six pulsars (SXP 51.0, SXP 152, SXP 214, SXP 323, SXP 327, SXP 504) along with SXP 565 and SXP 894 in some observations exhibit almost an eclipse-like sharp dip in their folded light curves (Figures 2–5). Such distinct features in the pulse profiles can be used to refine the period measurement (Section 3.2).

5.5. Spectral changes during pulsation cycles

Phase-resolved spectral analysis using quantile and energy versus phase diagrams reveals that many SXPs exhibit diverse spectral variations over the pulsation cycles. Two outstanding pulsars in this respect are SXP 172 in Figure 9 and SXP 214 (Hong et al. 2016). In the case of SXP 172, the quantile diagram shows that the overall photon indices vary significantly for an absorbed power-law model, and the energy versus phase diagram reveals that the dominant pulsation component comes from hard X-rays above 2 keV. In addition, SXP 18.3 and SXP 756 exhibit changes in the absorption during the pulsation cycles, whereas SXP 152 and SXP 304 show an intrinsic spectral variation, i.e., changes in the photon indices for absorbed power-law models. SXP 51.0, SXP 327 and SXP 565 show changes in both the absorption and photon index during the pulsation cycles.

The diverse pulse profile and spectral changes during pulsation phases observed in this analysis provide a rich data set for modeling the NS geometry and X-ray emission (e.g., Sasaki et al. 2012).

6. ACKNOWLEDGMENT

VA acknowledges financial support from NASA/Chandra grants GO3-14051X, AR4-15003X,

NNX15AR30G and NASA/ADAP grant NNX10AH47G. AZ acknowledges funding from the European Research Council under the European Union’s Seventh Framework Programme (FP/2007-2013)/ERC Grant Agreement n. 617001 and the MSCA-RISE-GA-691164 ”ASTRO-STAT” programme. PP acknowledges financial support from NASA contract NAS8-03060. MS acknowledges support by the the Deutsche Forschungsgemeinschaft through the research grant (SA 2131/4-1) and the Heisenberg professorship (SA 2131/5-1). SL acknowledges financial support from NASA/ADAP grant NNX14-AF77G.

Table 3
SMC pulsars

(1) Name	(2) Source (CXOU J)	(3) Pulsation Period (s)	(4) Orbital Period (d)	(5) LS Power	(6) False Prob. (10^{-x})	(7) Mod. Amp. (%)	(8) Pulsed Frac. (%)	(9) Net Counts 0.3–8 keV	(10) Median Energy (keV)	(11) Offset ($''$)	(12) Obs/ Each	(13) Stack	(14) Start Date (Y/M/D)	(15) GTIs (ks)	(16) Flag	(17) Obs. IDs (Deep Field ID)
SXP7.92	005758.40–722229.5	7.918130(50)	35.61	93.8	33.9	76(4)	58(7)	2878(54)	3.29(5)	1.2	3/2/1	1/1/1	13/09/06	48		15504 (08)
SXP18.3	004911.42–724936.9	18.36427(25) [†]	17.79	111.1	41.4	54(6)	35(7)	4466(67)	3.49(3)	0.5	2/2/1	1/1/1	14/01/15	48	a	15505 (09)
SXP51.0	004814.15–731003.6	50.6684(17) [†]		148.4	57.6	84(2)	74(4)	5947(77)	3.44(3)	0.3	3/1/1	2/1/1	13/03/04	45		14674 (11)
SXP59.0	005456.18–722647.9	58.8345(22) [†]	122	40.2	10.6	80(7)	67(12)	398(20)	2.0(2)	0.7	3/2/1	2/2/1	06/04/25	93	v	7155, 7327 (01A)
SXP138	005323.89–722715.5	138.924(10)	125	57.1	17.9	72(8)	54(12)	1357(37)	2.68(8)	0.1	2/2/2	1/1/1	06/04/25	93		7155, 7327 (01A)
SXP152	005750.41–720756.2	152.1063(94) [†]		87.6	31.2	76(4)	68(5)	4883(70)	2.75(4)	0.5	1/1/1	0/0/0	01/05/15	98	ei	1881
SXP172	005151.96–731033.9	171.848(20)	68.8	33.4	7.6	45(8)	25(9)	3263(57)	2.01(4)	0.5	3/3/1	1/1/1	06/11/21	96	i	8479, 7156, 8481 (02A)
SXP214	005011.26–730025.5	211.488(20)		274.4	112.3	96(3)	91(7)	1511(39)	3.84(5)	0.3	2/1/1	1/1/1	13/01/06	49	ev	14670 (07)
SXP304	010102.83–720659.2	304.542(66)	520	28.3	5.4	82(7)	66(14)	319(19)	2.2(1)	0.8	1/1/1	0/0/0	01/05/15	98		1881
SXP323	005044.69–731605.2	317.292(54)		51.9	15.7	75(6)	64(8)	2377(49)	2.73(6)	0.2	3/3/2	1/1/1	06/11/21	96	e	8479, 7156, 8481 (02A)
SXP327	005252.23–721715.3	326.813(31) [†]	45.99	193.0	76.9	69(3)	56(4)	9071(96)	2.34(3)	0.6	2/2/2	1/1/1	06/04/25	93	eia	7155, 7327 (01A)
SXP504	005455.88–724511.0	501.29(27)	269	53.7	16.4	65(8)	39(13)	1467(38)	3.04(8)	0.5	2/2/2	1/1/1	13/03/11	47		14669 (06)
SXP565	005455.85–724511.5	501.35(20) [†]		105.7	39.0	79(5)	63(9)	2060(46)	3.04(6)	1.1	2/2/2	1/1/1	13/08/26	45		15502 (06)
SXP701	005518.44–723851.8	726.31(44)	412	81.4	28.5	88(5)	76(11)	916(30)	2.96(6)	0.5	2/2/2	1/1/1	13/01/02	49	ia	14668 (05)
SXP756	005518.48–723852.4	728.11(57)		52.6	16.0	75(7)	57(13)	515(23)	2.8(1)	1.1	2/2/2	1/1/1	13/06/25	48		15501 (05)
SXP893	004942.02–723214.5	746.43(22) [†]	394	100.7	36.9	63(5)	38(7)	4194(65)	2.86(4)	0.1	4/3/3	1/1/1	06/11/21	96	a	8479, 7156, 8481 (02A)
SXP893	004929.80–731058.4	894.07(38) [†]		67.9	22.6	85(6)	77(9)	1464(39)	2.99(7)	0.4	6/6/5	3/3/3	06/11/21	96	e	8479, 7156, 8481 (02A)
SXP893	004929.63–731057.7	892.55(76)		65.4	21.6	81(6)	67(11)	1027(32)	3.16(9)	1.1	6/6/5	3/3/3	13/09/13	48	e	15507, 16367 (11)
<i>Marginal or Unusual Detection</i>																
SXP5.05	005702.12–722555.9	961.6(1.4)	17.2	25.0	4.0	18(3)	9(3)	34179(185)	3.39(1)	1.1	4/1/1	2/1/0	13/09/06	48	v	15504 (08)
SXP7.59?	003942.37–732427.4	3021(13)		28.1	5.4	19(3)	10(3)									
SXP8.02	010043.07–721133.4	7.58712(12)		17.5	17.5	58(11)	38(17)	151(12)	3.0(1)	-	2/2/1	0/0/0	13/01/18	44		14673 (10)
SXP74.7	004903.35–725052.2	8.018944(58)	33.3	18.0	10.5	31(7)	17(7)	5592(75)	1.349(7)	1.9	1/1/1	0/0/0	01/05/15	98		1881
SXP4693	005446.38–722522.9	24.9452(12)		18.9	4.5	56(12)	38(15)	912(30)	2.62(9)	0.2	2/2/1	1/1/1	13/01/17	44		14672 (09)
SXP4693	005446.38–722522.9	74.836(23) [†]		4.1	-	59(11)	39(14)	151(13)	2.3(2)	0.3	3/2/0	2/1/0	06/04/25	93		7155, 7327 (01A)
<i>No Pulsation Detection</i>																
SXP7.78	005205.88–722604.9		44.8			<100		73(9)	2.1(3)	1.3	2/2/0	1/1/0	06/04/25	93		7155, 7327 (01A)
SXP8.88	005153.05–723149.1					<67		182(15)	2.3(2)	1.0	2/2/0	1/1/0	06/04/25	93		7155, 7327 (01A)
SXP9.13	004913.53–731138.1		40.1			<26		1178(35)	2.91(7)	1.2	6/6/0	3/3/0	06/11/21	96		8479, 7156, 8481 (02A)
SXP15.3	004913.51–731137.4		74.3			<33		761(28)	2.97(9)	0.6	6/6/0	3/3/0	13/03/04	94		15507, 16367, 14674 (11)
SXP46.6	005213.93–731918.4		137.4			<62		213(15)	2.3(2)	0.6	3/3/0	1/1/0	06/11/21	96		8479, 7156, 8481 (02A)
SXP46.6	005355.37–722645.5					<100		64(8)	1.6(1)	0.3	2/2/0	1/1/0	06/04/25	93		7155, 7327 (01A)
SXP82.4	005209.01–723803.5		362			<100		18(5)	1.9(4)	0.5	5/2/0	1/1/0	13/08/26	45		15502 (06)
SXP140	005605.42–722200.0		197			<100		12(5)	2(1)	1.2	3/2/0	1/1/0	13/09/06	48		15504 (08)
SXP264	004723.40–731227.1		49.2			<28		1057(33)	2.70(8)	0.1	3/3/0	2/2/0	13/03/04	94		15507, 16367, 14674 (11)
SXP292	005047.98–731817.9					<100		20(5)	2.1(3)	0.2	3/2/0	1/1/0	06/11/21	42		8479 (02A)
SXP342	005403.87–722632.9					<100		17(5)	3.7(7)	0.2	2/2/0	1/1/0	06/04/26	47		7327 (01A)
SXP645	005535.14–722906.7					<48		355(19)	2.80(9)	0.7	3/3/0	2/2/0	13/01/02	97		14668, 15501 (05)

Notes – (1) Pulsar Name, (2) *Chandra* source Name, (3) Observed pulsation period, [†] indicates the refined periods by the EF method, (4) Orbital periods of the system (Coe & Kirk 2015), (5) The peak value of the LS periodogram, (6) False detection probability corresponding to the LS power, (7) Modulation Amplitude, (8) Pulsed fraction, (9) Net counts in 0.3–8 keV, (10) Median energy value of the source photons in 0.3–8 keV, (11) Offset between the *Chandra* source and the pulsar position reported in Coe & Kirk (2015) for SXP 8.02 and SXP 9.13 or Haberl & Sturm (2016) for the rest, (12) Number of individual observations, source detections and pulsation detections, (13) Same as (12) for the stacked observations, (14) Start date of the observation, (15) Good time intervals (GTIs), (16) Flags, "a": absorption variation during pulsation cycle, "i": intrinsic spectral variation during pulsation cycle, "e": eclipse-like feature in pulse profile, "v": flux variation, (17) Observation and Deep Field IDs. The numbers in parentheses represent 1σ equivalent errors.

Table 4
Spectral properties

(1) Name	(2) Net Counts 0.3–8 keV	(3) Hardness Ratio	(4) Median (keV)	(5) Quantile Analysis Ratio	(6) Γ or kT †	(7) nH	(8) Γ or kT ‡	(9) Spectral Fit nH	(10) χ^2_r / DoF	(11) 0.5–2 keV ($\times 10^{-13}$ erg cm $^{-2}$ s $^{-1}$)	(12) 2–8 keV ($\times 10^{-13}$ erg cm $^{-2}$ s $^{-1}$)	(13) Observed 0.5–8 keV	(14) L_X Intrinsic	(15) Obs. IDs (Deep Field ID)
SXP7.92	390(20)	0.52(5)	3.4(1)	1.11(5)	0.37	0.63	0.25(6)	0.1(2)	0.86 / 60	0.1(1)	2(2)	10.0(5)	10.4(5)	14671 (08)
SXP18.3	2878(54)	0.42(2)	3.29(5)	1.05(2)	0.35	0.33	0.25(6)	0.1(2)	0.86 / 60	1.3(1)	16(1)	75(6)	76(7)	15504 (08)
SXP51.0	4466(67)	0.57(1)	3.49(3)	1.14(7)	0.84	2.48	0.53(6)	2.5(3)	1.12 / 94	0.08(8)	0.8(8)	3.8(3)	4.4(3)	14672 (09)
SXP59.0	5947(77)	0.54(1)	3.44(3)	1.21(2)	0.62	2.61	0.50(5)	2.3(2)	0.87 / 98	2.1(1)	37(3)	170(12)	190(14)	15505 (09)
SXP138	1357(37)	0.23(3)	2.68(8)	0.98(4)	0.98	0.10	0.9(2)	0.3(5)	1.32 / 14	0.12(3)	0.7(2)	4(1)	4(1)	7155, 7327 (01A)
SXP152	4883(70)	0.25(1)	2.75(4)	1.03(1)	0.76	0.60	0.70(9)	0.3(2)	0.95 / 37	0.05(5)	0.2(2)	1.0(1)	2.9(4)	14671 (08)
SXP172	3263(57)	0.01(2)	2.01(4)	0.93(2)	0.85	1.28	0.76(4)	0.9(1)	1.02 / 76	1.16(7)	10.8(6)	52(3)	56(3)	1881
SXP214	1511(39)	0.67(3)	3.84(5)	1.46(4)	1.10	0.00	1.08(3)	0.00(2)	1.30 / 52	1.69(6)	6.7(2)	36(1)	37(1)	8479, 7156, 8481 (02A)
SXP304	319(19)	0.08(7)	2.2(1)	0.96(5)	0.95	0.37	0.9(2)	0.2(6)	0.58 / 11	0.10(3)	0.6(2)	3.0(9)	3(1)	14670 (07)
SXP323	2377(49)	0.26(2)	2.73(6)	1.04(2)	0.97	1.49	0.87(7)	1.0(2)	1.51 / 39	0.51(5)	4.3(4)	21(2)	23(2)	8479, 7156, 8481 (02A)
SXP327	9071(96)	0.12(1)	2.34(3)	1.02(1)	1.00	0.69	0.90(3)	0.37(7)	1.38 / 70	3.2(1)	20.1(8)	100(4)	107(4)	7155, 7327 (01A)
SXP504	1467(38)	0.38(3)	3.04(8)	1.12(2)	0.81	1.13	0.8(1)	1.3(4)	0.65 / 40	0.8(1)	8(1)	39(6)	43(7)	14669 (06)
SXP565	2060(46)	0.41(3)	3.04(6)	1.10(2)	0.76	0.63	0.60(8)	0.3(3)	0.91 / 43	1.4(2)	13(1)	61(7)	63(7)	15502 (06)
SXP701	2292(50)	-0.04(3)	1.94(3)	1.15(3)	1.40	1.59	1.16(7)	1.0(1)	1.06 / 47	0.63(5)	3.8(3)	19(2)	22(2)	1881
SXP756	2147(46)	0.39(2)	2.97(5)	1.16(2)	1.12	3.17	1.07(9)	2.8(4)	0.78 / 35	0.48(6)	5.0(7)	24(3)	29(4)	14671, 15504 (08)
SXP893	916(30)	0.38(3)	2.96(6)	1.16(4)	1.21	3.33	0.9(1)	2.2(6)	1.03 / 38	0.4(1)	5(1)	22(5)	26(6)	14668 (05)
SXP4693	515(23)	0.30(6)	2.8(1)	1.08(4)	1.02	1.63	1.0(2)	1.7(8)	0.59 / 20	0.26(8)	2.2(6)	10(3)	12(4)	15501 (05)
SXP74.7	4194(65)	0.30(2)	2.86(4)	1.06(2)	0.76	1.19	0.76(5)	1.1(2)	0.60 / 71	1.02(7)	10.0(7)	47(3)	52(4)	8479, 7156, 8481 (02A)
SXP8.02	1464(39)	0.39(3)	2.99(7)	1.10(2)	0.76	1.74	0.7(1)	1.6(5)	0.63 / 23	0.32(5)	3.6(6)	17(3)	19(3)	8479, 7156, 8481 (02A)
SXP7.59	509(23)	0.52(5)	3.18(8)	1.27(6)	1.09	3.39	0.6(1)	0.7(6)	0.68 / 28	0.6(6)	6(6)	30(1)	37(2)	14674 (11)
SXP7.78	1027(32)	0.42(4)	3.16(9)	1.12(3)	0.54	0.84	0.6(1)	0.7(6)	0.68 / 28	0.6(1)	6(1)	29(6)	30(6)	15507, 16367 (11)
SXP8.88	34179(185)	0.441(5)	3.39(1)	1.041(6)	0.20	0.00	0.17(1)	0.000(4)	1.37 / 145	14.61(8)	197(1)	911(5)	918(5)	15504 (08)
SXP9.13	151(12)	0.47(9)	3.0(1)	1.3(1)	1.74	7.01	1.4(4)	1(1)	0.60 / 5	0.06(6)	0.7(7)	3.2(3)	5.8(5)	14673 (10)
SXP15.3	308(18)	0.08(6)	2.1(1)	1.14(6)	1.73	1.99	‡0.39(6)	‡0.0(1)	1.15 / 43	‡3.01(7)	‡1.67(4)	‡20.1(5)	‡21.4(5)	15506 (10)
SXP292	5592(75)	-0.72(1)	1.349(7)	1.63(2)	‡1.13	‡0.72	‡3.7(6)	‡0.0(1)	0.55 / 24	0.50(9)	3.5(7)	17(3)	20(4)	14672 (09)
SXP46.6	912(30)	0.22(4)	2.62(9)	1.04(3)	1.09	1.25	1.0(1)	1.1(5)	0.03(3)	0.09(9)	0.6(6)	3.0(2)	5.0(4)	15505 (09)
SXP82.4	196(14)	0.25(8)	2.5(2)	1.19(9)	1.81	4.03	0.5(2)	0.0(9)	1.10 / 9	0.05(5)	0.2(2)	1.2(1)	2.5(2)	7155, 7327 (01A)
SXP140	151(13)	0.09(9)	2.3(2)	1.25(9)	2.08	4.51	0.5(2)	0.0(9)	0.14(4)	0.03(3)	0.2(2)	0.9(1)	0.9(1)	7155, 7327 (01A)
SXP264	73(9)	0.1(2)	2.1(3)	0.9(1)	0.80	0.00	0.1(1)	0.000(4)	0.83 / 24	0.07(7)	0.4(4)	2.0(2)	2.4(2)	7155, 7327 (01A)
SXP292	182(15)	0.1(1)	2.3(2)	1.08(8)	1.28	1.27	1.1(1)	2.9(5)	0.87 / 24	0.28(5)	3.0(5)	14(2)	17(3)	8479, 7156, 8481 (02A)
SXP342	1178(35)	0.37(3)	2.91(7)	1.13(3)	1.01	2.56	0.9(2)	1.9(8)	1.19 / 6	0.30(8)	2.9(8)	14(4)	16(4)	15507, 16367, 14674 (11)
SXP64.5	761(28)	0.41(4)	2.97(9)	1.18(3)	1.09	2.82	0.8(4)	0(2)	0.02(2)	0.09(7)	0.6(4)	3(2)	3(2)	8479, 7156, 8481 (02A)
SXP82.4	213(15)	0.16(7)	2.3(2)	1.01(6)	1.00	0.75	0.8(4)	0(2)	0.03(3)	0.04(4)	0.04(4)	0.32(4)	0.49(6)	7155, 7327 (01A)
SXP140	64(8)	-0.5(1)	1.6(1)	1.3(2)	2.19	1.01	1.0(1)	1.1(5)	0.06(6)	0.03(3)	0.06(6)	0.4(1)	0.4(1)	15502 (06)
SXP264	18(5)	-0.1(2)	1.9(4)	0.9(2)	1.10	0.00	1.0(1)	1.2(4)	0.75 / 35	0.01(1)	0.03(3)	0.18(7)	0.19(7)	15504 (08)
SXP292	12(5)	-0.2(3)	2(1)	0.5(3)	1.40	0.00	1.0(1)	1.2(4)	0.32(5)	0.01(1)	0.03(3)	0.26(7)	6(2)	8479 (02A)
SXP342	1057(33)	0.24(3)	2.70(8)	1.08(3)	4.04	1.62	0.5(2)	0.0(9)	0.01(1)	0.01(1)	0.2(2)	0.8(3)	0.8(3)	7327 (01A)
SXP64.5	20(5)	0.2(3)	2.1(3)	1.6(4)	1.08	12.02	0.5(2)	0.0(9)	1.10 / 9	0.14(4)	1.1(4)	5(2)	5(2)	14668, 15501 (05)
SXP82.4	17(5)	0.6(2)	3.7(7)	1.1(3)	-0.10	0.00	0.5(2)	0.0(9)	0.00(9)	0.14(4)	1.1(4)	5(2)	5(2)	14668, 15501 (05)

Notes – (1) Pulsar Name. (2) Net counts in 0.3–8 keV. (3) Mode of the posterior probability for Bayesian Enhanced Hardness Ratio (BHER). (4) Median energy value of the source photons in 0.3–8 keV. (5) Quartile ($E_{25\%}$ and $E_{75\%}$) ratio. (6) Quantile diagram based photon index (Γ) and (7) Extinction (N_{H} in 10^{22} cm $^{-2}$) estimate under an absorbed power-law model († for an absorbed thermal bremsstrahlung model). (8) Spectral model fit based photon index (Γ) and (9) Extinction (N_{H} in 10^{22} cm $^{-2}$) estimate under an absorbed power-law model (‡ for an absorbed two-temperature blackbody model). (10) Reduced χ^2 and Degrees of Freedom (DoF) of the fit. (11) Flux estimate in 0.5–2 keV and (12) in 2–8 keV. (13) Observed and (14) intrinsic luminosity estimates at 60 kpc. (15) Observation and Deep Field IDs.

Table 5
Phase resolved spectral analysis: SXP 18.3

(1)	(2)	(3)	(4)	(5)	(6)	(7)
Data	Net	Γ	N_{H}	χ_r^2 / DoF	L_{X}	
Segment	Count				Obs.	Int.
All	4466	$0.5^{+0.1}_{-0.1}$	$2.5^{+0.3}_{-0.3}$	1.12 / 94	$10.3^{+0.9}_{-0.9}$	$11.5^{+1.0}_{-1.0}$
<i>By folded phases</i>						
P0.15–0.35	1215	$0.5^{+0.1}_{-0.1}$	$3.2^{+0.9}_{-0.8}$	1.21 / 34	$14.7^{+3.2}_{-2.7}$	$16.4^{+3.6}_{-3.0}$
P0.70–1.00	1060	$0.7^{+0.1}_{-0.1}$	$2.3^{+0.6}_{-0.6}$	0.88 / 45	$7.6^{+1.5}_{-1.3}$	$8.5^{+1.7}_{-1.4}$

Notes.— (4) in 10^{22} cm^{-2} , (6) the observed and (7) intrinsic 0.5–8 keV X-ray luminosities in $10^{35} \text{ erg s}^{-1}$ at 60 kpc.

Table 6
Phase resolved spectral analysis: SXP 51.0

(1)	(2)	(3)	(4)	(5)	(6)	(7)
Data	Net	Γ	N_{H}	χ_r^2 / DoF	L_{X}	
Segment	Count				Obs.	Int.
All	6088	$0.5^{+0.0}_{-0.0}$	$2.3^{+0.2}_{-0.2}$	0.87 / 98	$16.9^{+1.2}_{-1.1}$	$18.7^{+1.4}_{-1.3}$
<i>By folded phases</i>						
P0.02–0.18	729	$0.9^{+0.2}_{-0.2}$	$3.1^{+0.8}_{-0.8}$	1.01 / 30	$10.8^{+2.8}_{-2.2}$	$12.9^{+3.3}_{-2.7}$
P0.18–0.47	1768	$0.4^{+0.1}_{-0.1}$	$2.3^{+0.6}_{-0.5}$	0.77 / 49	$17.3^{+2.8}_{-2.4}$	$19.0^{+3.0}_{-2.6}$
P0.47–0.60	254	$0.3^{+0.4}_{-0.3}$	$0.8^{+2.6}_{-0.9}$	0.93 / 8	$5.4^{+4.2}_{-1.7}$	$5.6^{+4.4}_{-1.7}$
P0.60–0.02	3337	$0.5^{+0.1}_{-0.1}$	$2.4^{+0.3}_{-0.3}$	1.07 / 69	$22.2^{+2.3}_{-2.1}$	$24.5^{+2.6}_{-2.3}$

Notes.— (4) in 10^{22} cm^{-2} , (6) the observed and (7) intrinsic 0.5–8 keV X-ray luminosities in $10^{35} \text{ erg s}^{-1}$ at 60 kpc.

Table 7
Phase resolved spectral analysis: SXP 152

(1)	(2)	(3)	(4)	(5)	(6)	(7)
Data	Net	Γ	N_{H}	χ_r^2 / DoF	L_{X}	
Segment	Count				Obs.	Int.
All	4883	$0.8^{+0.0}_{-0.0}$	$0.9^{+0.1}_{-0.1}$	1.02 / 76	$5.2^{+0.3}_{-0.3}$	$5.6^{+0.3}_{-0.3}$
<i>By folded phases</i>						
P0.10–0.65	3174	$0.7^{+0.1}_{-0.1}$	$0.9^{+0.2}_{-0.1}$	0.91 / 66	$6.2^{+0.5}_{-0.4}$	$6.7^{+0.5}_{-0.5}$
P0.75–0.90	587	$1.0^{+0.2}_{-0.1}$	$1.2^{+0.5}_{-0.5}$	1.17 / 23	$3.5^{+0.8}_{-0.6}$	$4.0^{+0.9}_{-0.7}$

Notes.— (4) in 10^{22} cm^{-2} , (6) the observed and (7) intrinsic 0.5–8 keV X-ray luminosities in $10^{35} \text{ erg s}^{-1}$ at 60 kpc.

Table 8
Phase resolved spectral analysis: SXP 172

(1)	(2)	(3)	(4)	(5)	(6)	(7)
Data	Net	Γ	N_{H}	χ_r^2 / DoF	L_{X}	
Segment	Count				Obs.	Int.
All	3289	$1.1^{+0.0}_{-0.0}$	$0.0^{+0.0}_{-0.0}$	1.30 / 52	$3.6^{+0.1}_{-0.1}$	$3.7^{+0.1}_{-0.1}$
<i>By folded phases</i>						
P0.30–0.70	1529	$0.8^{+0.0}_{-0.0}$	$0.0^{+0.0}_{-0.0}$	1.02 / 64	$4.6^{+0.2}_{-0.2}$	$4.7^{+0.2}_{-0.2}$
P0.75–0.25	1429	$1.4^{+0.1}_{-0.1}$	$0.0^{+0.1}_{-0.1}$	0.82 / 53	$2.7^{+0.2}_{-0.1}$	$2.8^{+0.2}_{-0.1}$

Notes.— (4) in 10^{22} cm^{-2} , (6) the observed and (7) intrinsic 0.5–8 keV X-ray luminosities in $10^{35} \text{ erg s}^{-1}$ at 60 kpc.

Table 9
Phase resolved spectral analysis: SXP 327

(1)	(2)	(3)	(4)	(5)	(6)	(7)
Data	Net	Γ	N_{H}	χ_r^2 / DoF	L_{X}	
Segment	Count				Obs.	Int.
All	9139	$0.9^{+0.0}_{-0.0}$	$0.4^{+0.1}_{-0.1}$	1.38 / 70	$10.0^{+0.4}_{-0.4}$	$10.7^{+0.4}_{-0.4}$
<i>By folded phases</i>						
P0.05–0.30	2843	$1.0^{+0.1}_{-0.1}$	$0.3^{+0.1}_{-0.1}$	1.06 / 61	$11.8^{+0.9}_{-0.8}$	$12.6^{+0.9}_{-0.8}$
P0.30–0.65	2996	$0.7^{+0.1}_{-0.1}$	$0.1^{+0.1}_{-0.0}$	1.21 / 76	$9.9^{+0.7}_{-0.6}$	$10.1^{+0.7}_{-0.6}$
P0.65–0.80	732	$0.8^{+0.1}_{-0.1}$	$0.2^{+0.4}_{-0.0}$	1.02 / 29	$5.4^{+1.0}_{-0.7}$	$5.6^{+1.1}_{-0.7}$
P0.80–0.05	2570	$1.0^{+0.1}_{-0.1}$	$0.7^{+0.2}_{-0.2}$	1.03 / 69	$11.1^{+1.0}_{-0.9}$	$12.1^{+1.1}_{-1.0}$

Notes.— (4) in 10^{22} cm^{-2} , (6) the observed and (7) intrinsic 0.5–8 keV X-ray luminosities in $10^{35} \text{ erg s}^{-1}$ at 60 kpc.

REFERENCES

Antoniou, V., & Zezas, A. 2016, MNRAS, 459, 528

Table 10
Phase resolved spectral analysis: SXP 565

(1)	(2)	(3)	(4)	(5)	(6)	(7)
Data	Net	Γ	N_{H}	χ_r^2 / DoF	L_{X}	
Segment	Count				Obs.	Int.
All	2292	$1.2^{+0.1}_{-0.1}$	$1.0^{+0.1}_{-0.1}$	1.06 / 47	$1.9^{+0.2}_{-0.1}$	$2.2^{+0.2}_{-0.2}$
<i>By folded phases</i>						
P0.05–0.55	1459	$1.3^{+0.1}_{-0.1}$	$1.4^{+0.2}_{-0.2}$	1.12 / 42	$2.2^{+0.2}_{-0.2}$	$2.7^{+0.3}_{-0.3}$
P0.60–1.00	668	$0.8^{+0.1}_{-0.1}$	$0.5^{+0.3}_{-0.2}$	0.87 / 27	$1.5^{+0.2}_{-0.2}$	$1.6^{+0.3}_{-0.2}$

Notes.— (4) in 10^{22} cm^{-2} , (6) the observed and (7) intrinsic 0.5–8 keV X-ray luminosities in $10^{35} \text{ erg s}^{-1}$ at 60 kpc.

Table 11
Phase resolved spectral analysis: SXP 756

(1)	(2)	(3)	(4)	(5)	(6)	(7)
Data	Net	Γ	N_{H}	χ_r^2 / DoF	L_{X}	
Segment	Count				Obs.	Int.
All	4211	$0.8^{+0.1}_{-0.1}$	$1.1^{+0.2}_{-0.2}$	0.60 / 71	$4.7^{+0.3}_{-0.3}$	$5.2^{+0.4}_{-0.3}$
<i>By folded phases</i>						
P0.45–0.70	1360	$0.8^{+0.1}_{-0.1}$	$1.8^{+0.5}_{-0.5}$	1.12 / 27	$6.2^{+1.1}_{-0.9}$	$7.0^{+1.2}_{-1.0}$
P0.70–0.45	2851	$0.8^{+0.1}_{-0.1}$	$0.8^{+0.2}_{-0.2}$	0.98 / 75	$4.2^{+0.4}_{-0.3}$	$4.5^{+0.4}_{-0.4}$

Notes.— (4) in 10^{22} cm^{-2} , (6) the observed and (7) intrinsic 0.5–8 keV X-ray luminosities in $10^{35} \text{ erg s}^{-1}$ at 60 kpc.

- Antoniou, V., Zezas, A., Hatzidimitriou, D., & Kalogera, V. 2010, ApJ, 716, L140
- Arumugasamy, P., Pavlov, G. G., & Kargaltsev, O. 2014, ApJ, 790, 103
- Christodoulou, D. M., Laycock, S. G. T., & Kazanas, D. 2017, arXiv:1704.06364
- Coe, M. J., Schurch, M., McBride, V. A., et al. 2009, MNRAS, 394, 2191
- Coe, M. J., Haberl, F., Sturm, R., et al. 2011, MNRAS, 414, 3281
- Coe, M. J., Bird, A. J., McBride, V., Bartlett, E. S., & Haberl, F. 2013a, The Astronomer's Telegram, 5547
- Coe, M. J., Bird, A. J., Kennea, J. A., et al. 2013b, The Astronomer's Telegram, 5662
- Coe, M. J., & Kirk, J. 2015, MNRAS, 452, 969
- Coe, M. J., Bartlett, E. S., Bird, A. J., et al. 2015, MNRAS, 447, 2387
- Corbet, R. H. D., Coe, M. J., Marshall, F. E., McBride, V. A., & Schurch, M. P. E. 2008, The Astronomer's Telegram, 1600
- Corbet, R. H. D., Markwardt, C. B., Coe, M. J., et al. 2003, The Astronomer's Telegram, 214
- Cowley, A. P., Schmidtke, P. C., McGrath, T. K., et al. 1997, PASP, 109, 21
- Cowley, A. P., & Schmidtke, P. C. 2003, AJ, 126, 2949
- Dickey, J. M., & Lockman, F. J. 1990, ARA&A, 28, 215
- Edge, W. R. T., Coe, M. J., & McBride, V. A. 2004a, The Astronomer's Telegram, 217
- Edge, W. R. T., Coe, M. J., & McBride, V. A. 2004b, The Astronomer's Telegram, 220
- Edge, W. R. T. 2005, Ph.D. Thesis, 727, Univ. Southampton
- Eger, P., & Haberl, F. 2008, A&A, 491, 841
- Finger, M. H., Ikhsanov, N. R., Wilson-Hodge, C. A., & Patel, S. K. 2010, ApJ, 709, 1249
- Freeman, P. E., Kashyap, V., Rosner, R., & Lamb, D. Q. 2002, ApJS, 138, 185
- Galache, J. L., Corbet, R. H. D., Coe, M. J., et al. 2008, ApJS, 177, 189–215
- Ghosh, P., & Lamb, F. K. 1979, ApJ, 234, 296
- Grindlay, J. E., Hong, J., Zhao, P., et al. 2005, ApJ, 635, 920
- Haberl, F., Eger, P., Pietsch, W., Corbet, R. H. D., & Sasaki, M. 2008, A&A, 485, 177
- Haberl, F., & Sturm, R. 2016, A&A, 586, A81
- Haberl, F., & Pietsch, W. 2004, A&A, 414, 667
- Haberl, F., Pietsch, W., Schartel, N., Rodriguez, P., & Corbet, R. H. D. 2004b, The Astronomer's Telegram, 219
- Haberl, F., Pietsch, W., Schartel, N., Rodriguez, P., & Corbet, R. H. D. 2004c, A&A, 420, L19
- Harris, J., & Zaritsky, D. 2004, AJ, 127, 1531
- Hilditch, R. W., Howarth, I. D., & Harries, T. J. 2005, MNRAS, 357, 304

- Hong, J., Schlegel, E. M., & Grindlay, J. E. 2004, *ApJ*, 614, 508
- Hong, J. S., van den Berg, M., Laycock, S., Grindlay, J. E., & Zhao, P. 2009, *ApJ*, 699, 1053
- Hong, J. 2012, *MNRAS*, 427, 1633
- Hong, J., van den Berg, M., Grindlay, J. E., Servillat, M., & Zhao, P. 2012, *ApJ*, 746, 165
- Hong, J., Antoniou, V., Zezas, A., et al. 2016, *ApJ*, 826, 4
- Horne, J. H., & Baliunas, S. L. 1986, *ApJ*, 302, 757
- Ikhsanov, N. R. 2007, *MNRAS*, 375, 698
- Ikhsanov, N. R., & Beskrovnaya, N. G. 2013, *Astronomy Reports*, 57, 287
- Ikhsanov, N. R., Kim, V. Y., Beskrovnaya, N. G., & Pustil'nik, L. A. 2013, *Ap&SS*, 346, 105
- Ikhsanov, N. R. 2012, *MNRAS*, 424, L39
- Illarionov, A. F., & Sunyaev, R. A. 1975, *A&A*, 39, 185
- Klus, H., Ho, W. C. G., Coe, M. J., Corbet, R. H. D., & Townsend, L. J. 2014, *MNRAS*, 437, 3863
- Kluźniak, W., & Rappaport, S. 2007, *ApJ*, 671, 1990
- Knigge, C., Coe, M. J., & Podsiadlowski, P. 2011, *Nature*, 479, 372
- Kozłowski, S., Onken, C. A., Kochanek, C. S., et al. 2013, *ApJ*, 775, 92
- Macomb, D. J., Fox, D. W., Lamb, R. C., & Prince, T. A. 2003, *ApJ*, 584, L79
- Marshall, F. E., Lochner, J. C., Santangelo, A., et al. 1998, *IAU Circ.*, 6818, 1
- McBride, V. A., Coe, M. J., Bird, A. J., et al. 2007, *MNRAS*, 382, 743
- Mori, K., Gotthelf, E. V., Zhang, S., et al. 2013, *ApJ*, 770, L23
- Lamb, R. C., Macomb, D. J., Prince, T. A., & Majid, W. A. 2002, *ApJ*, 567, L129
- Lamb, R. C., Fox, D. W., Macomb, D. J., & Prince, T. A. 2002, *ApJ*, 574, L29
- Laycock, S., Corbet, R. H. D., Coe, M. J., et al. 2005, *ApJS*, 161, 96
- Laycock, S., Zezas, A., Hong, J., Drake, J. J., & Antoniou, V. 2010, *ApJ*, 716, 1217
- Leahy, D. A., Darbro, W., Elsner, R. F., et al. 1983, *ApJ*, 266, 160
- Park, T., Kashyap, V. L., Siemiginowska, A., et al. 2006, *ApJ*, 652, 610
- Rajoelimanana, A. F., Charles, P. A., & Udalski, A. 2011, *MNRAS*, 413, 1600
- Rosen, S. R., Webb, N. A., Watson, M. G., et al. 2016, *A&A*, 590, A1
- Russell, S. C., & Dopita, M. A. 1992, *ApJ*, 384, 508
- Sasaki, M., Müller, D., Kraus, U., Ferrigno, C., & Santangelo, A. 2012, *A&A*, 540, A35
- Scargle, J. D. 1982, *ApJ*, 263, 835
- Scargle, J. D., Norris, J. P., Jackson, B., & Chiang, J. 2013, *ApJ*, 764, 167
- Schmidtke, P. C., & Cowley, A. P. 2005, *AJ*, 130, 2220
- Schmidtke, P. C., & Cowley, A. P. 2006, *AJ*, 132, 919
- Schmidtke, P. C., Cowley, A. P., Levenson, L., & Sweet, K. 2004, *AJ*, 127, 3388
- Shakura, N., Postnov, K., Kochetkova, A., & Hjalmarsdotter, L. 2012, *MNRAS*, 420, 216
- Shakura, N., Postnov, K., & Hjalmarsdotter, L. 2013, *MNRAS*, 428, 670
- Sturm, R., Haberl, F., Pietsch, W., et al. 2013, *A&A*, 558, A3
- Shtykovskiy, P., & Gilfanov, M. 2005, *MNRAS*, 362, 879
- Tiengo, A., Esposito, P., & Mereghetti, S. 2008, *ApJ*, 680, L133
- Udalski, A., & Coe, M. J. 2008, *The Astronomer's Telegram*, 1458
- Wang, J., & Chang, H.-K. 2012, *A&A*, 547, A27
- Wilms, J., Allen, A., & McCray, R. 2000, *ApJ*, 542, 914
- Yang, J., Laycock, S. G. T., Christodoulou, D. M., et al. 2017, *ApJ*, 839, 119
- Yokogawa, J., & Koyama, K. 1998, *IAU Circ.*, 6853, 2
- Yokogawa, J., Torii, K., Imanishi, K., & Koyama, K. 2000a, *PASJ*, 52, L37
- Yokogawa, J., Imanishi, K., Ueno, M., & Koyama, K. 2000b, *PASJ*, 52, L73
- Yokogawa, J., & Koyama, K. 1998, *IAU Circ.*, 6835, 2
- Zaritsky, D., & Harris, J. 2004, *ApJ*, 604, 167